UNIVERSITY OF OKLAHOMA

GRADUATE COLLEGE

SPECTROSCOPIC AND THEORETICAL STUDY OF LEAD MONOFLUORIDE TOWARD MEASURING THE PERMANENT ELECTRIC DIPOLE MOMENT OF THE ELECTRON

A DISSERTATION

SUBMITTED TO THE GRADUATE FACULTY

in partial fulfillment of the requirements for the

Degree of

DOCTOR OF PHILOSOPHY

By

TAO YANG
Norman, Oklahoma
2012

Downloaded from SHAREOK. Persistent Handle URL: https://hdl.handle.net/11244/319324

SPECTROSCOPIC AND THEORETICAL STUDY OF LEAD MONOFLUORIDE TOWARD MEASURING THE PERMANENT ELECTRIC DIPOLE MOMENT OF THE ELECTRON

A DISSERTATION APPROVED FOR THE
HOMER L. DODGE DEPARTMENT OF PHYSICS AND ASTRONOMY

BY

_____
Dr. Neil Shafer-Ray, Chair

_____
Dr. Eric Abraham

_____
Dr. Deborah K. Watson

_____
Dr. Brad Abbott

_____
Dr. Wai Tak Yip

© Copyright by TAO YANG 2012
All Rights Reserved.

谨以此论文，

献给我深爱的父母，

杨庆来和郑道琼，

我的岳父母，

王波和胡英，

以及我的妻子，

王小倩。

Acknowledgements

I would like to express my deepest gratitude to those people who help me in my pursuit toward my Ph.D. degree. Without you I would never complete my research goals step by step, and I would never develop my confidence, patience and creativity in my research career.

In the first place, I would like to thank Dr. Neil Shafer-Ray, for his excellent guidance, patience and caring. As my mentor and advisor, he encouraged me when I got discouraged by the experiment, broadened my knowledge when I got confused, and inspired my enthusiasm toward physics with his intuition and passion. Even he was away from the lab, he kept in contact with me and guided me through the whole process of writing the thesis. I can never finish my degree without him, and I can never wish an advisor more responsible than him.

I wish my sincere thanks to Dr. John Moore-Furneaux. He helped me a lot in my experimental progress while Neil was away. His smartness and humors helped me develop a positive attitude about research, and his invaluable technical skills made me enjoy working in the lab.

I would like to thank all my lab partners, James Coker, Haoquan Fan and Jeffrey Gillean. They participated actively in the lab, debated intensively over various kinds of problems and moved the research progress forward effectively. I also appreciate the efforts by post graduate students, Dr. Milinda Rupasinghe, Dr. Chris McRaven and Dr. Sivakumar Poopalasingam. They offered enormous useful suggestions when I joined Neil's group, and handed down a lab with a

very good shape.

Many thanks to Adrienne Wade in the electronic shop. She always found the exact parts what I looked for. Many thanks to Joel Young, Barry Bergeron and Sean Attebury in the machine shop. They provided a lot of beautiful home-made apparatuses of high quality. Many thanks to Debbie Barnhill, Danette Loyd, and Sharon Widner in the main office. They can always keep me away from the burden of the paperwork.

I would also express my thanks to Dr. Eric Abraham and his students, Parshuram Dahal, Sean Krzyzewski and Tom Akin. I benefited a lot from Eric's lab in my first year of research. And they are always generous in lending me lab equipments and sharing their research experiences.

I would like to thank Dr. Deborah K. Watson. I got a strong sense of achievement in her classes. I also thank Dr. Brad Abbott, and Dr. Wai Tak Yip. Thanks for your valuable time spent in proofreading my specialist and thesis.

I would also thank the chair of the department, Dr. Gregory Parker. He accepted me into the department and helped me a lot especially in my early days in the United States.

Again, I express my sincere gratitude to all of you who helped me to obtain my Ph.D. degree. Your encouragement and support will enlighten my way to success and I will proceed on without any hesitation.

Table of Contents

List of Tables viii

List of Figures xi

Abstract xii

1 Introduction 1
- 1.1 Why We Measure the e-EDM . . . 1
- 1.2 PbF as a Candidate for Measuring the e-EDM . . . 5
- 1.3 Organization of the Thesis . . . 10

2 Theoretical Evaluation of the Effective Spin-Rotational Hamiltonian 12
- 2.1 The Quantum Basis Set . . . 12
- 2.2 Effective Spin Model . . . 15
- 2.3 Evaluation of the Effective Spin-Rotational Hamiltonian . . . 16
- 2.4 Evaluation of the Field-dependent Hamiltonian . . . 23
- 2.5 Conclusion . . . 29

3 Determination of the Electric Dipole Moments of the X_1 and A States of the PbF Molecule 31
- 3.1 Introduction . . . 31
  - 3.1.1 Historic Progress toward PbF Spectroscopy . . . 31
  - 3.1.2 The difference between an edm and an EDM . . . 32
- 3.2 Effective Spin-Rotational Hamiltonian of PbF in the Presence of an External Electric Field . . . 34
- 3.3 Experiment . . . 39
- 3.4 Analysis . . . 42
- 3.5 Conclusion . . . 45

4 Design of Biased Stark Guides for Polar Molecules 46
- 4.1 Introduction . . . 46
- 4.2 Theory . . . 47
  - 4.2.1 Case 1: The helical guide. . . . 49
  - 4.2.2 Case 2: The Stark Gravitational Guide . . . 53
  - 4.2.3 Case 3: The Cylindrical Guide . . . 55
- 4.3 Summary of the Three Guides . . . 58
- 4.4 The Optical Double Resonance Quantum Beat Measurement of the e-EDM . . . 59
- 4.5 Estimate of the Statistical Sensitivity of the e-EDM Measurement . . . 63
- 4.6 Conclusion . . . 65

5 Comment on: Possibility of Zero-g-factor Paramagnetic Molecules for the Measurement of the Electron's Electric Dipole Moment 66
- 5.1 Introduction . . . 66

5.2 Theory 67
5.2.1 Effective Spin-Rotational Hamiltonian and the Choices of the Basic Sets in the Two Coordinate Frames 67
5.2.2 Field-free Effective Hamiltonian 69
5.2.3 Field-dependent Effective Hamiltonian 71
5.2.4 Evaluation of the g-factor 73
5.3 Conclusion 76

6 Summary **78**

References **80**

A Fabry-Pérot Interferometer **86**

List of Tables

1.1 Interaction energy between the e-EDM and the external magnetic and electric fields. 5
1.2 Current limits on EDM measurements. 7
1.3 Comparison between PbF and other e-EDM candidate diatomic molecules. 9

3.1 Sone examples of theoretically calculated and experimentally measured molecular dipole moments 34
3.2 Molecular dipole moments of X_1 and A states of $^{208}Pb^{19}F$, in comparison with the results from other work.(N.B. 1 Debye =0.3934 a.u.) . . 44

4.1 Estimate of the e-EDM statistical sensitivity of a 10-m-long guide. . . 64

List of Figures

1.1 An example of the demonstration for the CP-violation or the T-violation. 2

1.2 A method of measuring the elementary particle's EDM, such as an e-EDM. The solid line at the right is the transition when $\vec{E}||\vec{B}$, and the dashed line at the left is the transition when $-\vec{E}||\vec{B}$. The solid line at the center is the transition when there is no external electric field. This graph is adopted and modified from Dr. Eric Cornell's talk in 2010 Lepton Moments. 4

2.1 Hund case (c) angular momenta coupling scheme. In this scheme, **L** and **S** first couples to form the total electronic angular momentum $\mathbf{J}_e$, and the projection of $\mathbf{J}_e$ along the internuclear axis $\mathbf{S}'$ then couples with **R** to form the total angular moment **J**. The definitions of the angular momenta are introduced in the text. The figure is adopted and modified from Ref. [19]. 13

3.1 Comparison of the nature of edm and EDM. (a)Schematic representation of PbF in the molecular frame; (b)The rotating PbF molecule in the lab frame; (c)PbF molecules are aligned under the external electric field, where $\vec{d} \propto \vec{E}_{ext}$; (d)Molecular EDM inherited from the electron's spin, where $\vec{d}_e \propto \vec{S}$. 33

3.2 Left: Hyperfine level structure of the field-free Hamiltonian for X_1 and A states of $^{208}Pb^{19}F$ with F spanning from 0 to 2(unit is GHz). Here we treat the vibrational band origin energy as 0 for A state for convenience; Right: Field dependent level structure. The $Q_{fe}(1/2)$ transition is the desired e-EDM transition, which will be discussed in Chapter 4. 37

3.3 Experimental setup for spectroscopic measurement of $^{208}Pb^{19}F$ molecule. This is a similar experimental setup in Ref.[49]. 42

3.4 Field-dependent $X_1 \rightarrow A$ transitions of $^{208}Pb^{19}F$, with E=0.236 kV/cm, 0.393 kV/cm and 0.787 kV/cm, separately. The frequency detuning center for $R_{ff}(\frac{1}{2})$ transition is 686,484 GHz. For $P_{ee}(\frac{3}{2})$ it is 686,391 GHz. 43

4.1 (Color online) Two uniform field regions connected by various guides. In the envisioned experiment, a beam of molecules is polarized by laser radiation, guided by the field within the electrodes, and then probed with laser radiation. The guides shown are only 15 cm long, but guides exceeding 100 meters may be considered. 48

4.2 Relationship between the d/λ and the $V_o/(\lambda E_o)$ for the helical guide. Here voltages $\pm V_o$ are placed on the electrodes, d is the inner diameter of the guide, $\lambda = 2\pi/k$ is the pitch length, and E_o is the bias field of the guide. 50

4.3 Stark energy of the low-field seeking $X_1\ ^2\Pi_{1/2}(v = 0,\ F = 1,\ |M_F| = 1,\ J = 1/2,\ \Omega_+)$ state of $^{208}Pb^{19}F$. 51

4.4 (a) Simulated x-y trajectory of a particle as it moves $N = 4000\ twists =$ 100 m through the helical guide described in the text. (b) Accumulated geometric phase after a particle with the initial conditions described in the text travels from a uniform field region, through a helical guide of N turns, and exits into a second region of uniform field region. . . . 52
4.5 Cross section of the cylindrical guide. 55
4.6 Kepler-motion prediction of acceptance velocities of the cylindrical guide for the ground state of $^{198}Hg^{19}F$ (dashed line), $^{208}Pb^{19}F$(solid line), and $^{174}Yb^{19}F$(dotted line.) The shaded area indicates initial conditions of stable trajectories in a Monte Carlo Simulation assuming motion of high-field seeking ground-state $^{208}Pb^{19}F(v = 0,\ F = 1,\ |M_F| = 1,\ J = \frac{1}{2},\ \Omega_-)$ molecules governed by Eq. 4.8 and a potential energy $U(E)$ taken from a detailed calculation of the Stark interaction using known spectroscopic parameters. 58
4.7 Schematic for the optical double resonance quantum beat measurement of the e-EDM. 60
4.8 Ideal pattern of demodulated e-EDM signal of the reversing electric field. The solid line is the signal pattern for $\vec{E}||\vec{B}$, while the dashed line is the signal pattern for $-\vec{E}||\vec{B}$. 63

5.1 Comparison of the g-factors for the ground Ω-doublet state (upper line), the excited Ω-doublet state (lower line) and the analytical result (medium dashed line). J-state mixes from $\frac{1}{2}$ to $\frac{21}{2}$. 75

A.1 Schematic of the Fabry-Pérot Interferometer made of two mirrors. The mirrors are coated with film of high reflectivity. A monochromatic and collimated laser beam enters the etalon, with a small angle θ and near the co-axis of the two mirrors. 87
A.2 A typical plot of laser transmitted light intensity versus the detuning laser frequency. The laser frequency is detuned from 674,828.0 GHz. The mirror reflectivity is 90%, and the free spectral range for the etalon is 1 GHz. The transmitted laser light has a resolution of about 50 MHz. 89
A.3 The schematic of the etalon made of two confocal mirrors. The radius of the curvature of the mirror r is equivalent to the spacing d between the mirrors, therefore, the free spectral range is fixed by the choice of the mirrors. 90
A.4 The schematic of implementation of etalon in the measurement of the PbF spectroscopy. 91
A.5 A ideal plot of the transmitted fringes of the blue laser with the implementation of the EOPM. The modulation frequency is 100 MHz, therefore the sidebands are equally spaced by 100 MHz. The etalon has a FSR of 1 GHz, and the finesse $\mathcal{F}$ is 200. The number of the sidebands for each central fringe is determined by the modulation signal. The laser frequency is detuned from 674,828.0 GHz. 93

A.6 Doppler-free saturated absorption spectrum of $^{130}Te_2$ in $X_1(^3\Sigma_g) \rightarrow B_1(^3\Sigma_u)$ band near the frequency 674790.6 GHz. The pileups of the fringes are the derivative of the transmitted light intensity of the blue laser. Each pileup contains the major fringe and the four sidebands. Each pair of adjacent sidebands are spaced by 90 MHz. 94
A.7 Pressure-tuning of the etalon under the dispersion effect of the Nitrogen. The sideband is 40 MHz, which is applied on the probe beam of the Doppler-free saturated absorption setup. Adopted from *Cavity dispersion tuning spectroscopy of tellurium near 444.4 nm*, Coker *et al.*, J. Opt. Soc. Am. B 28, December 2011. 96

Abstract

The existence of the electron's permanent electric dipole moment (e-EDM) would break the charge-parity symmetry and time-reversal symmetry. This existence can not only explain some fundamental physical phenomena in our Universe, but also would help in searching new physics beyond the Standard Model. The search for the e-EDM then becomes one of the fundamental problems in physics. Numerous experimental efforts have been made and a recent result set an upper limit of $|d_e| < 1.05 \times 10^{-28} e{\cdot}\text{cm}$ in an e-EDM measurement, while the Standard Model predicts a value of $|d_{e,SM}| < 10^{-38} e{\cdot}\text{cm}$. This new upper limit does not imply a non-zero e-EDM, therefore the intense competitions over the non-zero e-EDM measurement are still going-on.

The experiments searching for an e-EDM in atoms and molecules are carried out in different approaches. The heavy diatomic molecule lead monofluoride(PbF) has several advantages over the other candidates for measuring an e-EDM. It has a large internally polarized electric field, an extremely small magnetic g-factor varying with external electric field, close-spaced energy levels with two opposite parities, and the ability to suppress emotional magnetic field.

Based on these features, a unique detection scheme called pseudo-continuous resonant enhanced multiphoton ionization (pc-REMPI) is utilized to determine the spectrum of the PbF molecule. In this thesis, I report the molecular electric dipole moments of the X_1 and A states of the PbF molecule by analyzing the optical spectra of the $X_1 \rightarrow A$ transition in the presence of an applied electric

field. The result will contribute to the further studies about the high resolution state-sensitive transition. All of these should rely on the fully understanding of the matrix elements of the Hamiltonian of the ground state X_1 and A state. In addition, the implementation of a biased Stark guide will enhance the coherence time by several orders of magnitude, which lays the foundation for an optical double resonance quantum beat measurement of the e-EDM. Finally, this thesis includes a re-examination of a theoretical prediction published in 2006 that the $^{208}Pb^{19}F$ molecule may exhibit a specific electric field at which the magnetic g-factor vanishes. Such a situation might have led to an e-EDM measurement immune to the background magnetic field. The work here, based on vastly improved spectroscopy of the molecule, shows that this situation does not occur in $^{208}Pb^{19}F$. With the quality magnetic shielding, it is proved that the $^{208}Pb^{19}F$ molecule is still a qualified candidate for measuring the e-EDM.

Chapter 1

Introduction

In this chapter, I will address the importance of measuring the electron's electric dipole moment (e-EDM) and its relation to the violation of the charge-parity symmetry and the violation of the time-reversal symmetry. Historic progress toward the e-EDM measurement is briefly reviewed, and the features of the PbF molecule in our e-EDM measurement will be discussed.

1.1 Why We Measure the e-EDM

The Standard Model states that there are three basic types of forces that mediate the interactions: electromagnetic, strong and weak nuclear. Each of these interactions has its unique properties associated with the three discrete symmetries: Charge conjugation (C-symmetry), parity inversion (P-symmetry) and time-reversal (T-symmetry). Since 1950 extensive theoretical work and experiments have been done to investigate the violations of these symmetries.

Perhaps the first suggestion of the violation of the discrete symmetries was proposed by E. M. Purcell and N. F. Ramsey in 1950. They suggested the possibility of the existence of an electric dipole moment for the elementary particles and nuclei, and pointed out that such a dipole moment would imply P- and T-violation[1]. However, there was no experimental evidence to prove the violations of the discrete symmetries. In 1956, T. D. Lee and C. N. Yang pointed

out the P-symmetry is violated in the weak interaction[2]. This suggestion was soon verified by C. S. Wu and her co-workers in the beta decay of Cobalt-60[3]. In 1964, J. Cronin, V. Fitch and their coworkers demonstrated that CP-symmetry is broken in the decay of the long-lived neutral Kaons[4]. Because of the validity of the CPT invariance for the time of the thesis that has been written, the violation of the CP-symmetry is equivalent to the violation of the T-reversal symmetry[5]. These results of CP-violation or T-violation are consistent with the complex phase appearing in the quark mixing matrix in the Standard Model. This CP-violating or T-violating phase would imply that the magnitude of the e-EDM should be less than $10^{-38}e\cdot$cm[6]. Therefore, the existence of the electric dipole moments for the elementary particles is suggested to be measured[1]. The following figure is a simple demonstration of why the existence of an e-EDM would produce CP-violation, however, the existence of e-EDM is not the only factor that contributes to CP-violation[7].

Assume a group of electrons with the internal spin $\frac{1}{2}$ has a magnetic dipole moment $\vec{\mu}$ and an e-EDM $\vec{d_e}$, and is influenced by the external magnetic field $\vec{B}$ and the electric field $\vec{E}$. The schematic is shown in Fig.1.1.

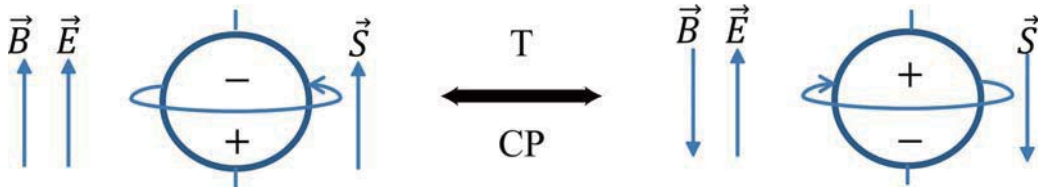

Figure 1.1: An example of the demonstration for the CP-violation or the T-violation.

The interaction energy can be written in a nonrelativistic form as

$$U = -\vec{\mu} \cdot \vec{B} - \vec{d_e} \cdot \vec{E}. \tag{1.1}$$

Under the CP-symmetry, $\vec{E}$ is invariant since $\vec{E}$ reverses its sign under both the C- and the P-symmetry. $\vec{B}$ is invariant under the P-symmetry but changes its sign under the C-symmetry. Since the weak interaction affects all fermions, we have to assume that $\vec{d_e}$, as well as $\vec{\mu}$, should obey the Pauli exclusion principle and align or anti-align with the direction of $\vec{S}$. Therefore, $\vec{d_e}$ and $\vec{\mu}$ flip their signs under the CP-symmetry. Then the new interaction energy under the CP-transformation will be represented as

$$U = -\vec{\mu} \cdot \vec{B} + \vec{d_e} \cdot \vec{E}, \tag{1.2}$$

which is different from what we get before the CP-transformation.

Actually, this example also implies a naive but straightforward way to measure the e-EDM(Fig.1.2). The elementary particle such as an electron is located in a uniform $\vec{B}$ and $\vec{E}$ field, with the $\vec{E}$ field flipping parallel-aligned or anti-parallel-aligned to the applied $\vec{B}$ field. If without the applied electric field, the interaction energy of the electron's spin and the applied magnetic field will be

$$U = \frac{1}{2}|g_e|\mu_B B \tag{1.3}$$

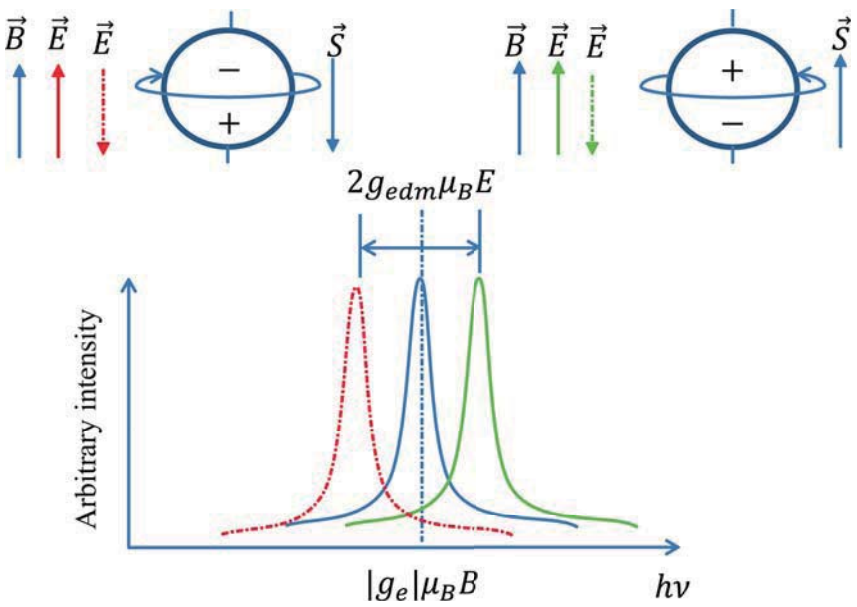

Figure 1.2: A method of measuring the elementary particle's EDM, such as an e-EDM. The solid line at the right is the transition when $\vec{E}||\vec{B}$, and the dashed line at the left is the transition when $-\vec{E}||\vec{B}$. The solid line at the center is the transition when there is no external electric field. This graph is adopted and modified from Dr. Eric Cornell's talk in 2010 Lepton Moments.

and

$$U = -\frac{1}{2}|g_e|\mu_B B. \tag{1.4}$$

Where μ_B is the Bohr magneton. Eq. 1.3 is for the situation when $\vec{B}$ is parallel to $\vec{S}$ and Eq. 1.4 is for the situation when $\vec{B}$ is anti-parallel to $\vec{S}$. Thus a spontaneous emission of a photon will be generated for this two-level system, with the energy of $|g_e|\mu_B B$. After the electric field is applied, the interaction energy can be listed as the Table 1.1. If we flip $\vec{E}$ back and forth, we can show

	$\vec{B} \parallel \vec{S}$	$\vec{B} \parallel -\vec{S}$
$\vec{E} \parallel \vec{S}$	$U = \frac{1}{2}\|g_e\|\mu_B B + \frac{1}{2}g_{edm}\mu_B E$	$U = -\frac{1}{2}\|g_e\|\mu_B B + \frac{1}{2}g_{edm}\mu_B E$
$\vec{E} \parallel -\vec{S}$	$U = \frac{1}{2}\|g_e\|\mu_B B - \frac{1}{2}g_{edm}\mu_B E$	$U = -\frac{1}{2}\|g_e\|\mu_B B - \frac{1}{2}g_{edm}\mu_B E$

Table 1.1: Interaction energy between the e-EDM and the external magnetic and electric fields.

the two spontaneous transitions with the transition energies as

$$\begin{aligned} \Delta U &= \frac{1}{2}|g_e|\mu_B B + \frac{1}{2}g_{edm}\mu_B E - (-\frac{1}{2}|g_e|\mu_B B - \frac{1}{2}g_{edm}\mu_B E) \\ &= |g_e|\mu_B B + g_{edm}\mu_B E, \end{aligned} \tag{1.5}$$

and

$$\Delta U = |g_e|\mu_B B - g_{edm}\mu_B E. \tag{1.6}$$

Here, we use $d_e = \frac{1}{2}g_{edm}\mu_B$ in analogy to the magnetic g-factor, but g_{edm} is not dimensionless in this situation. Therefore, the hunt for tracing the origins of the CP-violation now turns into the measurement of d_e, or equivalently, g_{edm} of the fermions.

1.2 PbF as a Candidate for Measuring the *e*-EDM

The candidates for measuring the fundamental particles' EDMs can be the elementary particles such as an electron and a muon, or the composite particles such as a proton, a neutron, an atom or even a molecule. In general, the search for the elementary particles' EDMs can be divided into two major groups: Leptonic EDMs and Hadronic EDMs. Leptonic EDM measurement involves sources

including the paramagnetic atoms like Thallium, or the paramagnetic molecules such as PbF, YbF, ThO, HfF^+, PbO, etc. It also includes a diamagnetic atom source ^{199}Hg. Hadronic EDM measurement involves sources such as a neutron, a proton, a deuteron, etc. As N. Ramsey pointed out[1], searching for an EDM of an electrically charged particle showed significant insensitivity and the neutral particles were more favorable choices. Ramsey and his collaborators worked on the neutron's EDM and first reported the upper limit of the neutron EDM as $|d_n| < 5 \times 10^{-20} e{\cdot}$cm[8]. In 2006, the newest upper bound for d_n is $|d_n| < 2.9 \times 10^{-26} e{\cdot}$cm, increased by a factor of 10^6 in over 50 years[9]. This is the current upper limit for the Hadronic EDM measurement. In 2011, Hudson's group set an upper limit on $|d_e| < 1.05 \times 10^{-28} e{\cdot}$cm for an e-EDM measurement[10], which is for the Leptonic EDM measurement. The Standard Model predicts an e-EDM, however, smaller than $10^{-38} e{\cdot}$cm. Despite of the great difficulties in measuring the EDMs, there are an number of groups all over the world working on the first measurement of the non-zero value of the EDMs. Table 1.2 shows some selected elementary particles' EDM limits.

Our group use the PbF as the probe for measuring e-EDM. As a diatomic molecule, PbF shares some similar advantages over the atoms as the other polar molecules in several aspects. First, PbF gains a large internally polarized electric field induced by the external electric field. According to the Schiff's theorem, a neutral system in the presence of an external electric field will experience no acceleration on average. Therefore, the non-pointlike constituents of the

Particle	Experimental system	Measured EDM limit(e·cm)	Standard Model prediction(e·cm)	New physics prediction(e·cm)
Electron	YbF	1.05×10^{-28}[10]	10^{-38}[7]	10^{-26} SUSY [11]
Quark Sector	Neutrons	2.9×10^{-26}[9]	10^{-32}[12]	$10^{-25} \sim 10^{-28}$[7][13]
Quark Sector	^{199}Hg	3.1×10^{-29}[14]	10^{-33}[14]	10^{-28} SUSY[14]

Table 1.2: Current limits on EDM measurements.

.

system should be rearranged in order to completely screen out the effect of the external field, E_{ext}[15]. This would imply that no neutral system can be sensitive to an e-EDM to the first order in perturbation theory. For heavy polar molecules, however, composite electrons move in a combination of both electric and strong magnetic fields. For this case, the Schiff's theorem does not apply. In the same paper that Schiff introduced his theorem, he pointed out that not only does this theorem not apply to heavy atoms, but also such atoms will have a sensitivity to an e-EDM that is hundreds of times larger than that of a bear electron[15]. Later, Sanders showed that heavy paramagnetic molecules are even more sensitive to a possible e-EDM than the heavy atoms[16]. The sensitivity of a molecular system to an e-EDM is often quoted in terms of an effective internal field, E_{int}, so that $U_{edm} = -\vec{d_e} \cdot \vec{E}_{int}$. Table 1.3 shows E_{int} for some of the most promising e-EDM candidates. The ground state of the molecule PbF has $E_{int} = -31 \times 10^9$ V/cm, a value more than sufficient to gain sensitivity to an e-EDM measurement.

The second advantage is that PbF is a g-2 e-EDM system. The magnetic g-factor of the PbF molecule of the ground state changes with the external electric field, and there exists an electric field where the magnetic moment is very small (approximately 0.04). This feature will make the PbF molecule, especially ^{208}Pb^{19}F, immune to the background magnetic field. The background magnetic field will mimic as an e-EDM signal, and add difficulties to the e-EDM measurement. This small g-factor as well as the high quality magnetic shielding

Molecule	e-EDM sensitive state	E_{eff} (GV/cm)	g-factor	Polarization field (kV/cm)	Radiative lifetime (ms)	Published limit $10^{-27} e$·cm
PbF	Ground $^2\Pi_{\frac{1}{2}}$	-31[24][25]	$g-2$	6(even) 0.2(odd)	-	-
Tl	Excited $6P_{1/2}$,F=1	0.04[26]	g	100[27]	-	1.6(90% C.L.)[27]
YbF	Ground $^2\Sigma^+_{\frac{1}{2}}$	32±3[28]	g	10[10]	-	1.05(90% C.L.)[10]
a(1) PbO	Metastable $^3\Sigma^+$	26.2[29]	g	10[30]	0.01[30]	-
BaF	Ground $^2\Sigma^+_{\frac{1}{2}}$	6.1±0.8[31]	g	-	-	-
HgF	Ground $^2\Sigma^+_{\frac{1}{2}}$	99[24][25]	g	-	-	-
WC	Ground $^3\triangle_1$	54[32]	$g-2$	0.001[33]	-	-
HfF^+	Ground $^3\triangle_1$	30[25]	$g-2$	< 0.01	500[34]	-
ThO	Metastable $H^3\triangle_1$	104[25]	$g-2$	< 0.01	1.0[25]	-

Table 1.3: Comparison between PbF and other e-EDM candidate diatomic molecules.

will greatly reduce the influence coming from the magnetic field.

The third advantage PbF possesses is that its ground state has two close-spaced energy levels of two opposite parities[17]. The low-lying F=1 ground states of $^{207}Pb^{19}F$ are near-degenerated and requires a two orders of magnitude smaller electric field to polarize the states than $^{even}Pb^{19}F$. Even for $^{even}Pb^{19}F$, the required field to fully polarize the molecule is still obtainable in a laboratory environment.

The fourth advantage of our candidate, like the other heavy diatomic molecules for measuring the e-EDM, is its suppression ability of the emotional magnetic field effect[28]. In our e-EDM measurement, we create a supersonic molecular beam which is rotationally cooled. This supersonic beam of the molecules will induce a $\vec{v} \times \vec{E}$ effect, and the resulting relativistic magnetic field adds nontrivial systematic error to the molecular experiments. With its large enhancement factor and strong tensor polarizability, PbF can suppress the $\vec{v} \times \vec{E}$ effect. All of these beneficial properties lay a solid foundation for us to track the footprints of the e-EDM.

1.3 Organization of the Thesis

In Chapter 2, I will derive the matrix elements of the Hamiltonian for the ground state of the $^{208}Pb^{19}F$ molecule using an effective-spin model. The energy level structure of the A state of the $^{208}Pb^{19}F$ molecule can also be determined in a similar way. In the next chapter, I will talk about the measurement of the

molecular dipole moments of the electronic ground state $X_1(\upsilon = 0)$ and the electronic excited $A(\upsilon = 1)$ state for $^{208}Pb^{19}F$, in a pc-REMPI detection scheme. In Chapter 4, I will address the focusing and guiding properties of various two-dimensional Stark guides, which are used for guiding polar molecules while conserving the M state alignment of the molecules. An optical double resonance quantum beat measurement of the e-EDM will be proposed, and the statistical sensitivity of the experiment will be estimated under this system. In Chapter 5, I will comment on the impact of a sign error in the possibility of using zero-g-factor paramagnetic molecules to measure the electron's electric dipole moment. In the last chapter, I will summarize all and make a brief conclusion for the work toward the e-EDM measurement using the PbF molecule.

Chapter 2

Theoretical Evaluation of the Effective Spin-Rotational Hamiltonian

In this chapter, I will construct the effective spin-rotational Hamiltonian, based on the effective spin model, and give the the general representation for the matrix elements of the PbF molecule, especially for the ground state of the $^{208}Pb^{19}F$ molecule. This chapter will provide a solid basis for Chapter 3 and Chapter 5.

2.1 The Quantum Basis Set

The evaluation of the PbF energy level structure will originate from constructing the Hamiltonian, and the determination of the matrix elements of the Hamiltonian is based on the related wave function, or in other words, the quantum basis set. We can start from studying the coupling schemes of the various angular momenta which can be classified by Hund's coupling cases[18].

The total wave function of a molecule can be expressed by its well-defined internal quantum numbers. For the PbF molecule which has one free electron, it is the Hund's case (c) molecule, assuming that the interaction between the nuclear rotation and the total electronic motion is much smaller than the interaction between the electron orbital and the electron spin. This can be represented by the following scheme Fig. 2.1

In Fig. 2.1, the electronic orbital angular momentum **L** strongly couples

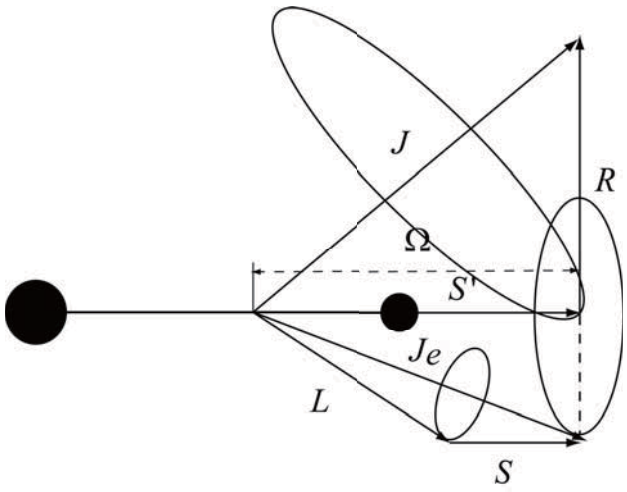

Figure 2.1: Hund case (c) angular momenta coupling scheme. In this scheme, **L** and **S** first couples to form the total electronic angular momentum $\mathbf{J}_e$, and the projection of $\mathbf{J}_e$ along the internuclear axis $\mathbf{S}'$ then couples with **R** to form the total angular moment **J**. The definitions of the angular momenta are introduced in the text. The figure is adopted and modified from Ref. [19].

with the electronic spin angular momentum **S** to form a resultant electronic total angular momentum $\mathbf{J}_e$. $\mathbf{J}_e$ precesses rapidly along the internuclear axis and therefore has a well-defined projection Ω. In Hund's case (a), **L** and **S** strongly couples with the internuclear axis first and have well-defined projection Λ and Σ, which couples to form Ω ($\Omega = \Lambda + \Sigma$). In Hund's case (c), Λ and Σ are not well-defined but Ω is well-defined. A well-define quantum number means that it is a good quantum number and its relevant operator commutes with the Hamiltonian. Kozlov *et al.*[44] proposed the concept the effective spin $\mathbf{S}'$, whose eigenvalue is Ω. This effective spin model will greatly simplify the calculation of the matrix elements which will be described later. Then $\mathbf{S}'$ couples with the rotational angular momentum of the nuclei **R** to form the total angular

momentum **J**. If one or two nuclei have the nuclear spin (for ^{208}Pb^{19}F, ^{19}F has a nuclear spin $I = \frac{1}{2}$), it will couple with **J** to form the new total angular momentum **F** (**F** is not labeled in Fig. 2.1). In the absence of the external electric and magnetic field, the complete quantum basis set for describing the ^{208}Pb^{19}F molecule in the molecular frame would be[19]

$$|S_{F,\Omega}\rangle = |FIJM_F\Omega\rangle. \tag{2.1}$$

There are two points we need to pay close attention here. This quantum basis set is good for the molecule-based coordinate system. It is no longer a basis for the lab-based coordinate system because it is not an eigenstate of the total wave function and the quantum basis set of a definite space parity needs to be constructed. Fortunately, this transition from the molecule-based basis to the lab-based basis can be completed by the rotation matrix associated with the Euler angles. The molecule-based coordinate system and the related total wave function will be effective only when we calculate the matrix elements of the Hamiltonian which does not associate with the space parity, for example, the field-dependent Hamiltonian. Also, there are no absolute well-defined quantum numbers or good quantum numbers. Most of the good quantum numbers are rigorously good to different levels of the coupling effects. For example, the total angular momentum **J** is neither good in the case of the existence of the external electric field or magnetic field, nor in the presence of the nuclear spin

(hyperfine effect). Although the $^{208}Pb^{19}F$ molecule is not pure Hund's case (c) for all possible J's, Eq. 2.1 is a quantum basis set good enough to be employed in determining the $^{208}Pb^{19}F$ molecule's rotational structure, fine structure and hyperfine structure. For each level of the coupling effects, we need to slightly modify the quantum basis set and evaluate carefully its relevant Hamiltonian.

2.2 Effective Spin Model

In order to construct the energy level structure, we need to analyze the various contributions of the coupling effects, write out the matrix elements and evaluate the eigenenergies. Simply put, we can imagine the $^{208}Pb^{19}F$ molecule as a rigid rotor. The Hamiltonian can be expressed as[20]

$$H = H_0 + B_v \mathbf{R}^2, \tag{2.2}$$

where H_0 represents the Hamiltonian of a specific non-degenerate electronic state and non-degenerate vibrational state (vibronic state), and B_v is the rotational constant for the vibrational state v. From Eq. 2.2 we rewrite the rotational Hamiltonian as (abandon the vibrational quantum number v since we focus on

a specific vibronic state)[44]

$$H_{rot} = B\mathbf{R}^2 \tag{2.3}$$

$$= B(\mathbf{J} - \mathbf{S}')^2 \tag{2.4}$$

$$= B\mathbf{J}^2 - \Delta\mathbf{S}' \cdot \mathbf{J} + B\mathbf{S}'^2. \tag{2.5}$$

Here Δ is the Ω-doubling constant that is a measurable constant and defined in Ref. [44]. Because the ground state of the ^{208}Pb^{19}F molecule is $^2\Pi_{1/2}$(the general notation is $^{2S+1}\Lambda_\Omega$) and it is the Hund's case (c) state, the coupling between the effective spin and the total electronic angular momentum will remove the degeneracy of the rotational structure. Later I will discuss more about the function of the effective spin $\mathbf{S}'$ in evaluating the matrix elements of the rotational Hamiltonian.

2.3 Evaluation of the Effective Spin-Rotational Hamiltonian

From the Born-Oppenheimer approximation, the exact total wave function for a diatomic molecule in the molecule-based frame can be expressed as[21]

$$\psi \approx \psi_{elec}\psi_{vib}\psi_{rot}\psi_{espin}\psi_{nspin}, \tag{2.6}$$

and this will yield the separation of the field-free Hamiltonian

$$H \approx H_{elec} + H_{vib} + H_{rot-fs} + H_{hf}. \tag{2.7}$$

Here, ψ_{elec} is the electronic wave function, ψ_{vib} is the vibrational wave function, ψ_{rot} is the rotational wave function, ψ_{espin} is the electron spin wave function, ψ_{nspin} is the nuclear spin wave function, H_{elec} is the electronic Hamiltonian, H_{vib} is the vibrational Hamiltonian, H_{rot-fs} is the rotational Hamiltonian including the fine structure, which is Eq. 2.3, and H_{hf} is the hyperfine interaction Hamiltonian. Since we focus on a specific vibronic state, we can prove that $H_{elec}+H_{vib}$ is actually H_0 in Eq. 2.2. Honestly, H_0 is not necessarily included in calculating the matrix element of the total Hamiltonian since it always appears in the diagonal terms, and we can add the energy T_v to the energy level structure to simplify our formalism.

First let's consider the rotational Hamiltonian. The arbitrary rotation operator about $\hat{n}$ by an angle a we have (Eq. 3.23 in Ref. [20])

$$\mathbf{R}_n(a) = \exp\left(-\imath a \mathbf{J}\cdot\hat{\mathbf{n}}\right), \tag{2.8}$$

where $\mathbf{J}\cdot\hat{\mathbf{n}} = -\imath\frac{\partial}{\partial a}$. It is easily demonstrated that $\mathbf{J}^2$ commutes with the rotation operator $\mathbf{R}_n(a)$ for an arbitrary rotation , therefore the value of J is unchanged, but the rotation can still alter the projection of the angular momentum along a lab-based axis. Hence, after a three-dimensional rotation of

the Euler angles (ϕ, θ, χ)(Page 245 in Ref. [19]), the rotational wave function $|JM_J\rangle$ will be projected into a linear combination of the states $|JM'_J\rangle$ and written as

$$\mathbf{R}(\phi, \theta, \chi)|JM_J\rangle = \sum_{M'_J} D^J_{M'_J M_J}(\phi, \theta, \chi)|JM'_J\rangle. \tag{2.9}$$

Here, $D^J_{M'_J M_J}(\phi, \theta, \chi)$ is the rotation matrix or the Wigner D-matrix, and reversely we have

$$\begin{aligned} D^J_{M'_J M_J}(\phi, \theta, \chi) &= \langle JM'_J|\mathbf{R}(\phi, \theta, \chi)|JM_J\rangle \\ &= e^{-\imath\phi M'_J} d^J_{M'_J M_J}(\theta) e^{-\imath\chi M_J}. \end{aligned} \tag{2.10}$$

Here, $d^J_{M'_J M_J}(\theta) = \langle JM_J|e^{-\imath\theta J_Y}|JM_J\rangle$, whose algebraic expressions can be obtained from Page 89 in Ref. [20]. Subsequently, the rotational wave function for a symmetric top (which satisfies the Hund's case (c) coupling scheme) is given by (Eq. 3.125 in Ref. [20])

$$|JM_J\Omega\rangle = (\frac{2J+1}{8\pi^2})^{1/2} D^{J*}_{M\Omega}(\phi, \theta, \chi). \tag{2.11}$$

It can be proved that Eq. 2.11 is the simultaneous eigenfunction for $\mathbf{J}^2$, J_Z (projection in the lab-based frame is M_J) and J_z (projection in the molecule-based frame is Ω). The matrix elements of the rotational Hamiltonian can then be expressed as

$$\langle J'M'_J\Omega'|B\mathbf{J}^2|JM_J\Omega\rangle = BJ(J+1)\delta_{JJ'}\delta_{M_J M'_J}\delta_{\Omega\Omega'}, \tag{2.12}$$

where $\mathbf{J}^2$ is expressed as[20]

$$\mathbf{J}^2 = -\frac{\partial^2}{\partial\theta^2} - \cot\theta\frac{\partial}{\partial\theta} - \frac{1}{\sin^2\theta}(\frac{\partial^2}{\partial\phi^2} + \frac{\partial^2}{\partial\chi^2} - 2\cos\theta\frac{\partial^2}{\partial\phi\partial\chi}). \tag{2.13}$$

The second term is the effective spin-rotational term, and the matrix elements can be expressed as

$$\langle J'M'_J\Omega'| - \Delta\mathbf{S}'\cdot\mathbf{J}|JM_J\Omega\rangle = -\Delta\sum_{t=-1}^{1}(-1)^t\langle J'M'_J\Omega'|J'^1_t S'^1_{-t}|JM_J\Omega\rangle. \tag{2.14}$$

Here, the effective spin spherical tensor of rank 1 is related to the usual raising and lowering operators in the usual way

$$S'^1_q = \begin{cases} S'_z & q = 0 \\ \mp\frac{1}{\sqrt{2}}(S'_x \pm \imath S'_y) & q = \pm 1. \end{cases} \tag{2.15}$$

Then we can get

$$\langle J'M'_J\Omega'| - \Delta\mathbf{S}'\cdot\mathbf{J}|JM_J\Omega\rangle = -\Omega'\Delta\sqrt{1+(\Omega-\Omega')^2}\langle J'M'_J\Omega'|J'^1_{\Omega-\Omega'}|JM_J\Omega\rangle. \tag{2.16}$$

Here, please note that $\mathrm{J}'^1_{\Omega-\Omega'}$ refers to the angular momentum in the molecule-based frame and we can apply the Wigner rotation matrix to make it from an

operator in the lab-based frame

$$\langle J'M'_J\Omega'|J'^1_t|JM_J\Omega\rangle = \langle J'M'_J\Omega'|\sum_s D^1_{st}J^1_s|JM_J\Omega\rangle. \tag{2.17}$$

We note that the expectation value of the Wigner rotation matrix can be expressed by a rank-1 tensor

$$\langle J'M'_J\Omega'|D^1_{st}|JM_J\Omega\rangle = (-1)^s\langle J'M'_J\Omega'|T^1_{-s}(t)|JM_J\Omega\rangle, \tag{2.18}$$

thus we can have

$$\begin{aligned}\langle J'M'_J\Omega'|J'^1_t|JM_J\Omega\rangle &= \sum_s \langle J'M'_J\Omega'|(-1)^s T^1_{-s}(t)J^1_s|JM_J\Omega\rangle \\ &= \frac{\delta_{JJ'}\delta_{M_JM'_J}}{2J+1}(J'M'_J\Omega'||J^1||JM_J\Omega)(J'M'_J\Omega'||T^1(t)||JM_J\Omega),\end{aligned} \tag{2.19}$$

where

$$(J'M'_J\Omega'||J^1||JM_J\Omega) = \delta_{JJ'}\sqrt{J(J+1)(2J+1)} \tag{2.20}$$

and

$$(J'M'_J\Omega'||T^1(t)||JM_J\Omega) = (-1)^{J'+\Omega+1}\sqrt{(2J+1)(2J'+1)}\begin{pmatrix} J' & 1 & J \\ \Omega' & t & -\Omega \end{pmatrix}, \tag{2.21}$$

both of which are derived from the Wigner-Eckart theorem (Page 180 in Ref. [20]). In the end, the matrix elements of the effective spin-rotational Hamiltonian

will be expressed as

$$\begin{aligned}\langle J'M'_J\Omega'|-\Delta\mathbf{S}'\cdot\mathbf{J}|JM_J\Omega\rangle &= \delta_{JJ'}\delta_{M_JM'_J}\Omega'\Delta\sqrt{1+(\Omega-\Omega')^2}\\ &\times\sqrt{J(J+1)(2J+1)}\\ &\times(-1)^{J'+\Omega+1}\begin{pmatrix} J' & 1 & J\\ \Omega' & \Omega-\Omega' & -\Omega\end{pmatrix}\\ &= -\delta_{JJ'}\delta_{M_JM'_J}(\frac{\Delta}{4}\delta_{\Omega\Omega'}+\frac{\Delta}{2}(J+\frac{1}{2})\delta_{\Omega-\Omega'}).\end{aligned} \tag{2.22}$$

If the nuclear spin of the ^{19}F is added, then M_J is not a good quantum number but M_F is. The molecular basis set is therefore the Eq. 2.1, and in a further step we have

$$\begin{aligned}|S_{F,\Omega}\rangle &= |FIJM_F\Omega\rangle\\ &= (2F+1)^{1/2}\sum_{M_J,M_I}(-1)^{J-I+M_F}\begin{pmatrix} J & I & F\\ M_J & M_I & -M_F\end{pmatrix}\times|S_{JI}\rangle,\end{aligned} \tag{2.23}$$

where $|S_{JI}\rangle = |JM_J\Omega\rangle|\Omega\rangle|IM_I\rangle$. Because our final goal is to represent the matrix elements of the Hamiltonian in the lab-based coordinate frame, the construction of the quantum basis set in the lab-based frame is especially demanded. Therefore, the molecular wave function of the ^{208}Pb^{19}F will be

writen in terms of the symmetric top wave functions of definite parity p

$$\begin{aligned} |S_{F,p}\rangle &= |FIJM_F p\rangle \\ &= |S_{F,\Omega=1/2}\rangle + p(-1)^{J-1/2}|S_{F,\Omega=-1/2}\rangle \\ &= \frac{1}{\sqrt{2}}(|FIJM_F, \Omega = \frac{1}{2}\rangle + p(-1)^{J-1/2}|FIJM_F, \Omega = -\frac{1}{2}\rangle). \end{aligned} \tag{2.24}$$

For convenience, we introduce the total parity

$$\chi = (-1)^F p \tag{2.25}$$

and another sign q

$$q = 2(J - F), \tag{2.26}$$

and we can prove that

$$q\chi = p(-1)^{J-1/2}, \tag{2.27}$$

which leads to

$$S_{F,\chi} = \frac{1}{\sqrt{2}}(|FIJM_F, \Omega = \frac{1}{2}\rangle + q\chi|FIJM_F, \Omega = -\frac{1}{2}\rangle). \tag{2.28}$$

This helps us to label the allowed transition in our PbF spectrum. For example, when we label the $X_1(J, p) \rightarrow A(J', p')$ transition, there will be six branches: $R_{ee}(J)$, $R_{ff}(J)$, $P_{ee}(J)$, $R_{ff}(J)$, $Q_{ef}(J)$, and $Q_{fe}(J)$. Here, R, P and Q indicates $J' = J + 1, J - 1$ and J. The first subscript indicates the sign of the product $q'\chi'$ for the A states and the second subscript indicates the sign of the

product $q\chi$ for the ground state. Also, e indicates $q'\chi' = 1$ or $q\chi = 1$, while f indicates $q'\chi' = -1$ or $q\chi = -1$. Under these definitions, the matrix elements of the rotational and the Ω-doubling Hamiltonian will be rewritten as

$$\begin{aligned}\langle S_{F',\chi'}|B\mathbf{J}^2 - \Delta\mathbf{S}'\cdot\mathbf{J}|S_{F,\chi}\rangle = \delta_{qq'}\delta_{\chi\chi'}\delta_{FF'}\delta_{M_F M'_F}[BJ(J+1) - D_{rot}(J(J+1))^2 \\ -q\chi\frac{\Delta}{2}(J+\frac{1}{2})],\end{aligned} \tag{2.29}$$

where we remove the constant term $-\Delta/4$ and add a centrifugal distortion term $-D_{rot}(J(J+1))^2$. Note the term $B\mathbf{S}'^2$ produces a constant term $B\Omega^2$ which can also be removed.

The evaluation of the matrix elements of the hyperfine structure can be proceeded in a similar way, which can be reviewed elsewhere[22][49]. Here I simply surrender the result

$$\begin{aligned}\langle S_{F',\chi'}|\mathbf{I}\cdot\hat{A}\cdot\mathbf{S}'|S_{F,\chi}\rangle = \delta_{\chi\chi'}\delta_{FF'}\delta_{M_F M'_F}[-(\frac{\chi A_\perp}{4} + \frac{A_\parallel + \chi A_\perp}{4(2F+1)}q)\delta_{q,q'} \\ + \frac{A_\parallel + \chi A_\perp}{2}(\frac{\sqrt{F(F+1)}}{2F+1})]\delta_{q,-q'},\end{aligned} \tag{2.30}$$

where $A_\parallel$ and $A_\perp$ are the hyperfine constants which can be determined from the PbF molecular spectrum.

2.4 Evaluation of the Field-dependent Hamiltonian

The e-EDM measurement using the PbF molecule is performed under the interaction with the external electric field and magnetic field, as demonstrated

in Chapter 1. Here I will derive the magnetic Zeeman interaction for the $^{208}Pb^{19}F$ first. The interaction Hamiltonian is represented as

$$\begin{aligned} H_B &= \mu_B \mathbf{B}' \cdot \hat{G} \cdot \mathbf{S}' \\ &= \mu_B \sum_t (-1)^t G'^1_{-t} B'^1_t, \end{aligned} \tag{2.31}$$

with $G'^1_t = -(gS'^{1}_t + L'^{1}_t)$, $B'^1_0 = B'_z$, and $B'^1_{\pm 1} = \mp\frac{1}{\sqrt{2}}(B'_x \pm \imath B'_y)$.

Here, the prime sign means that the operators are in the molecule-based frame, and g is the gyromagnetic ratio which indicates the ratio between the magnetic dipole moment and its relative angular momentum. Note the difference between S'^{1}_t and S'^1_t. The former one means the electron spin operator of the rank-1 tensor in the molecule-based frame while the other one means the effective spin operator of the rank-1 tensor in the molecule-based frame. Also, the tensor $\hat{G}$ gives the strength of the Zeeman interaction and is diagonal in the molecular frame. We define two magnetic constants $G_\parallel$ and $G_\perp$ as

$$\begin{cases} G_\parallel S'^1_0 = G'^1_0 \\ G_\perp S'^1_\pm = G'^1_\pm. \end{cases} \tag{2.32}$$

To define the molecular orbital of the unpaired electron of the PbF molecule, we have

$$\begin{cases} \phi_{1/2} = \sum_{l=1}^{\infty} [c^l_0 |l,0\rangle|\frac{1}{2}\rangle + c^l_1 |l,1\rangle|-\frac{1}{2}\rangle] \\ \phi_{-1/2} = \sum_{l=1}^{\infty} [c^l_0 |l,0\rangle|-\frac{1}{2}\rangle + c^l_1 |l,1\rangle|\frac{1}{2}\rangle], \end{cases} \tag{2.33}$$

where the general form of $|l,0\rangle|\frac{1}{2}\rangle$ is related to $|l,m_l\rangle|m_s\rangle$, with l relating to the orbital angular momentum, m_l relating to the projection of the orbital angular momentum along the internuclear axis, and m_s relating to the projection of the spin angular momentum along the internuclear axis. c_0^l and c_1^1 are the expansion coefficients. $\phi_{1/2}$ and $\phi_{-1/2}$ represent the molecular orbitals of the unpaired electron with the projection of the effective spin along the internuclear axis as $\Omega = \pm\frac{1}{2}$. For convenience, we use $|\pm\frac{1}{2}\rangle$ to represent $\phi_{1/2}$ and $\phi_{-1/2}$ but do not mix with $|m_s\rangle$ term which is closely associated with $|l,m_l\rangle$. Based on these definitions, we can have

$$\begin{cases} \langle\frac{1}{2}|G_0'^1|\frac{1}{2}\rangle = \langle\frac{1}{2}|G_\parallel S_0'^1|\frac{1}{2}\rangle = \frac{1}{2}G_\parallel \\ \langle-\frac{1}{2}|G_\pm'^1|\frac{1}{2}\rangle = \langle-\frac{1}{2}|G_\perp S_{\pm1}'^1|\frac{1}{2}\rangle = \frac{1}{\sqrt{2}}G_\perp. \end{cases} \tag{2.34}$$

Here, we use the raising and lowering relation in Eq. 2.15. In this way, we can get the definitions of the $G_\parallel$ and $G_\perp$

$$\begin{cases} G_\parallel = 2\langle\frac{1}{2}|G_0'^1|\frac{1}{2}\rangle = -2\langle\frac{1}{2}|G_0'^1|-\frac{1}{2}\rangle \\ G_\perp = \sqrt{2}\langle-\frac{1}{2}|G_{-1}'^1|\frac{1}{2}\rangle = -\sqrt{2}\langle\frac{1}{2}|G_{+1}'^1|-\frac{1}{2}\rangle. \end{cases} \tag{2.35}$$

Now let's evaluate the matrix element of the Hamiltonian of the Zeeman effect

in absence of the hyperfine structure and in the molecule-based frame

$$\begin{aligned}\langle J'M'_J\Omega'|H_B|JM_J\Omega\rangle &= \mu_B\langle J'M'_J\Omega'|\sum_t(-1)^t G'^1_{-t}B'^1_t|JM_J\Omega\rangle \\ &= \mu_B\langle J'M'_J\Omega'|\sum_{s,t}(-1)^t G'^1_{-t}D^1_{st}B^1_s|JM_J\Omega\rangle \\ &= \mu_B\sum_{s,t}(-1)^t\langle J'M'_J\Omega'|D^1_{st}|JM_J\Omega\rangle\langle\Omega'|G'^1_{-t}|\Omega\rangle B^1_s.\end{aligned} \tag{2.36}$$

From Eq. 2.11, we have

$$\begin{aligned}\langle J'M'_J\Omega'|D^1_{st}|JM_J\Omega\rangle &= \frac{\sqrt{(2J+1)(2J'+1)}}{8\pi^2}\int D^{*J}_{M_J\Omega}D^{J'}_{M_{J'}\Omega'}D^1_{st}d\omega \\ &= \sqrt{(2J+1)(2J'+1)}(-1)^{2J'-2+M_J+\Omega}\begin{pmatrix} J' & 1 & J \\ M'_J & s & -M_J\end{pmatrix} \\ &\times\begin{pmatrix} J' & 1 & J \\ \Omega' & t & -\Omega\end{pmatrix}.\end{aligned} \tag{2.37}$$

From here, we can have

$$\begin{aligned}\langle J'M'_J\Omega'|H_B|JM_J\Omega\rangle &= \mu_B \sum_{s,t} (-1)^t G_t B^1_s \begin{pmatrix} 1/2 & 1/2 & 1 \\ \Omega & -\Omega' & -t \end{pmatrix} \times \alpha_{1/2}(-1)^{1/2-\Omega'} \\ &\quad [(2J+1)(2J'+1)]^{1/2}(-1)^{J'+M_J+J'+\Omega}(-1)^{J'+J+1-J+M_J} \\ &\quad \times (-1)^{J-M_J} \begin{pmatrix} J & 1 & J' \\ -M_J & s & M'_J \end{pmatrix} \begin{pmatrix} J' & 1 & J \\ \Omega' & t & -\Omega \end{pmatrix} \\ &= \mu_B \sum_{s,t} (-1)^{J+J'-1/2-M_J} G_t B^1_s \sqrt{\frac{3}{2}(2J+1)(2J'+1)} \\ &\quad \begin{pmatrix} 1/2 & 1 & 1/2 \\ \Omega' & t & -\Omega \end{pmatrix} \begin{pmatrix} J' & 1 & J \\ \Omega' & t & -\Omega \end{pmatrix} \begin{pmatrix} J & 1 & J' \\ -M_J & s & M'_J \end{pmatrix},\end{aligned} \tag{2.38}$$

where $\alpha_\Omega = \sqrt{\Omega(\Omega+1)(2\Omega+1)}$. Note that these are the matrix elements of the Zeeman interaction in the molecule-based frame, and the matrix elements for a definite parity state including the hyperfine structure in the lab-based

frame is[22]

$$\begin{aligned}\langle F'I'J'M'_F p'|H_B|FIJM_F p\rangle &= \mu_B\delta_{pp'}\delta_{II'}\sqrt{(2F+1)(2F'+1)(2J+1)(2J'+1)}\\ &\times\frac{(-1)^{I+F'+J'}}{2}\begin{Bmatrix} J' & F' & I\\ F & J & 1\end{Bmatrix}(\frac{1}{J_<+1}+\frac{\delta_{JJ'}}{J})^{1/2}\\ &\times[(J'-J-\frac{\delta_{JJ'}}{2J+1})\frac{G_\parallel}{2}-p(-1)^{J-1/2}\frac{G_\perp}{2}]\\ &\times B^1_{M_F-M'_F}(-1)^{F'-M_F}\begin{pmatrix} F' & 1 & F\\ -M'_F & M'_F-M_F & M_F\end{pmatrix},\end{aligned} \tag{2.39}$$

where $J_< = max(J, J')$. Similarly, we can get the matrix element of the Stark interaction in the molecule-based frame[62]

$$\begin{aligned}\langle J'M'_J\Omega'|H_E|JM_J\Omega\rangle &= \langle J'M'_J\Omega'|-D\mathbf{E}'\cdot\mathbf{n}'|JM_J\Omega\rangle\\ &= DE(-1)^{J+\Omega}\sqrt{(2J+1)(2J'+1)}\times(-1)^{J'-M'_J}\\ &\times\begin{pmatrix} J' & 1 & J\\ \Omega' & 0 & -\Omega\end{pmatrix}\begin{pmatrix} J' & 1 & J\\ -M'_J & 0 & M_J\end{pmatrix},\end{aligned} \tag{2.40}$$

where D is the dipole moment of the PbF molecule, $\mathbf{n}$ is the molecular internuclear axis and $\mathbf{E}$ is the external electric field. Generally, the Stark interaction

of the PbF molecule follows closely that of the Zeeman case[22], which is

$$\begin{aligned}\langle F'I'J'M'_F p'|H_E|FIJM_F p\rangle = \delta_{p,p'}\delta_{II'}\sqrt{(2F+1)(2F'+1)(2J+1)(2J'+1)} \\ \times \frac{(-D)(-1)^{I+F'+J'}}{2}(\frac{1}{J_<+1}+\frac{\delta_{JJ'}}{J})^{1/2} \\ \times (J'-J-\frac{\delta_{JJ'}}{2J+1})E^1_{M_F-M'_F}(-1)^{F'-M_F} \\ \times \begin{pmatrix} F' & 1 & F \\ -M'_F & M'_F-M_F & M_F \end{pmatrix} \begin{Bmatrix} J' & F' & I \\ F & J & 1 \end{Bmatrix}\end{aligned} \tag{2.41}$$

2.5 Conclusion

In summary, the matrix elements of the ground state Hamiltonian of the ^{208}Pb^{19}F molecule have been derived in both molecule-based frame and lab-based frame, where

$$H = B\mathbf{J}^2 - \Delta\mathbf{S}'\cdot\mathbf{J} + \mathbf{I}\cdot\hat{A}\cdot\mathbf{S}' - D\mathbf{E}\cdot\mathbf{n} + \mu_B\mathbf{B}\cdot\hat{G}\cdot\mathbf{S}'. \tag{2.42}$$

Here the first term is the usual rotational energy, the seconde term gives the Ω-doubling energy and is written in terms of the effective spin that gives the projection of the total angular momentum along the internuclear axis, the third term is the hyperfine energy due to the nuclei of the ^{19}F, the fourth term is the Stark interaction, and the last term gives the Zeeman interaction. We usually assign the prime sign to indicate the operators in the molecule-based frame,

which can be transferred from the multiplication of the rotation matrices and the operators in the lab-based frame. The matrix elements for each term of the Hamiltonian lay a solid foundation for determining the energy level structure of the $^{208}Pb^{19}F$ molecule, which is of great importance to the detection of the e-EDM sensitive transition.

Chapter 3

Determination of the Electric Dipole Moments of the X_1 and A States of the PbF Molecule

This chapter presents a measurement of the molecular dipole moments of the electronic ground state X_1 and the electronic excited state A of $^{208}Pb^{19}F$. This measurement is carried out by analyzing the optical spectra of the $X_1 \rightarrow A$ transition in the presence of an applied electric field. To interpret this Stark spectra, the energy level structure of the X_1 and A states are numerically analyzed using an effective spin-rotational model. By comparing the result of the analysis to an observed quadratic dependence of the Stark shifts with respect to the applied field, the dipole moments of the X_1 and A states are determined. I conclude with a discussion of the observed molecular dipole moments for the implications in the e-EDM measurements.

3.1 Introduction

3.1.1 Historic Progress toward PbF Spectroscopy

PbF is an e-EDM candidate for its large enhancement factor and large internally induced electric field[16]. The spectroscopic study of the lead monofluoride molecule began in the 1930s. The vibrational spectral analysis of PbF was initially performed by Frank Morgan[35] and G. D. Rochester[36][37]. During the following decades, the vibrational and rotational energy level structures

were measured at higher resolution by several groups[38][39][40]. In 1976 D. J. W. Lumley and R. F. Burrow determined the rotational constants for $^{208}Pb^{19}F$. Meanwhile, the theoretical calculations of the spectral structures had been studied as well. The hyperfine structures of PbF molecule have been studied by R. A. Frosch and H. M. Foley[41][42]. More recently, Kozlov and his collaborators gave a full description of the effective spin-rotational Hamiltonian of the PbF molecule in the electronic state $|\Omega| = \frac{1}{2}$, as well as the field dependent terms[24][43][44].

3.1.2 The difference between an edm and an EDM

The measurement of the dipole moment is critical to the design of any molecular e-EDM experiment. Although other groups have measured dipole moments for a variety of e-EDM sensitive molecules, our group is the first to measure the molecular dipole moments of PbF. A natural question is what is the difference between the usual molecular electric dipole moment (edm) and the CP-violating electric dipole moment (EDM). Diatomic molecules usually have a molecular dipole moment due to the different electronegativities of the two atoms (Fig. 3.1(a)). This "permanent" dipole moment is fixed in the molecular frame but not in the lab frame. Because the rotational motion of the molecule conserves parity, the molecular frame dipole moment averages to zero in the lab frame (Fig. 3.1(b)). Certainly, an applied electric field may mix the states of the opposite parities, align the polar molecule and reveal an edm proportional to

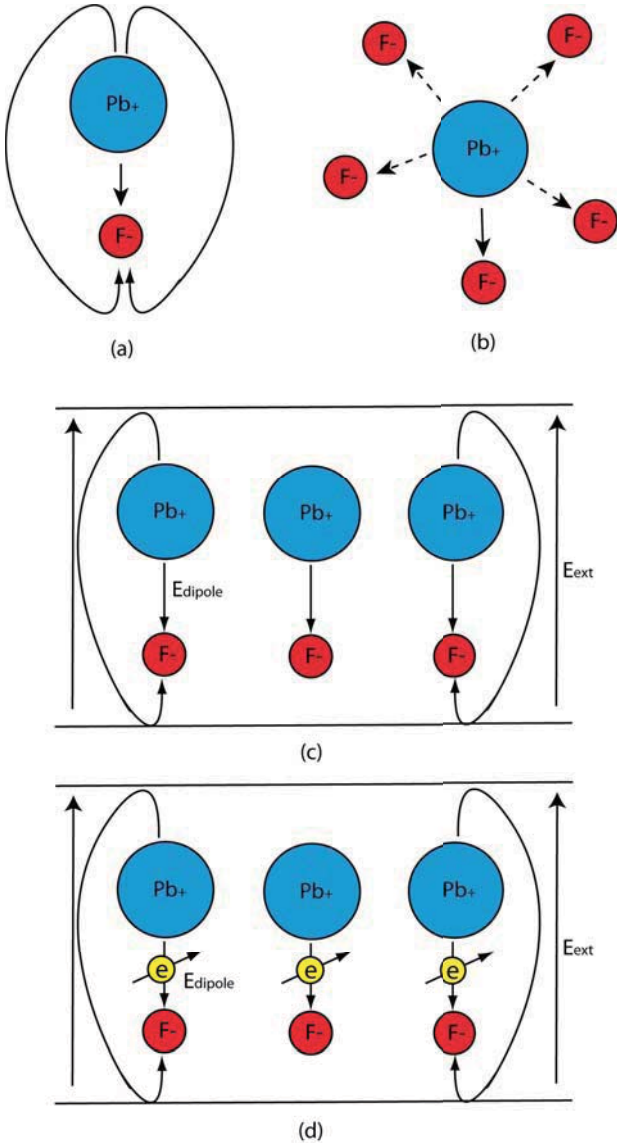

Figure 3.1: Comparison of the nature of edm and EDM. (a)Schematic representation of PbF in the molecular frame; (b)The rotating PbF molecule in the lab frame; (c)PbF molecules are aligned under the external electric field, where $\vec{d} \propto \vec{E}_{ext}$; (d)Molecular EDM inherited from the electron's spin, where $\vec{d_e} \propto \vec{S}$.

the applied field (Fig. 3.1(c)). Table 3.1 shows some calculated and measured molecular dipole moments of heavy diatomic molecules.

On the other hand, the extremely small EDM, or e-EDM, is associated with

Molecule	State	Theory (Debye)	Experiment(Debye)
^{174}YbF	$X^2\Sigma^+(\upsilon = 0)$ $A^2\Pi_{1/2}(\upsilon = 0)$		3.91(4) [45] 2.48(3) [46]
HgF	$X^2\Sigma_{1/2}$ $A^2\Pi_{1/2}$	4.15 [44] 2.75 [24]	
BaF	$X^2\Sigma_{1/2}$	2.93 [31]	3.17 [47]

Table 3.1: Sone examples of theoretically calculated and experimentally measured molecular dipole moments

the electron's spin, and can only exist for P,T-odd interactions. Whereas as a conventional edm creates a dipole field proportional to an external field, an EDM creates a (extremely small) dipole field proportional to the molecule's spin angular momentum (Fig. 3.1(d)). This exotic EDM would therefore produce an electric dipole, not by an electric field, but when its angular moment is aligned, either optically or with a magnetic field.

3.2 Effective Spin-Rotational Hamiltonian of PbF in the Presence of an External Electric Field

Here I start from a numerical analysis of the effective spin-rotational Hamiltonian and carry out the simulation of the Stark energy shifts which are sensitive to the molecular dipole moments of $X_1(\upsilon = 0)$ and $A(\upsilon = 1)$ states.

We know that the Born-Oppenheimer approximation treats the electronic Hamiltonian and the nuclear Hamiltonian separately[23], which will yield a spin-rotational wavefunction. This simplification helps to denote the molecular

Hamiltonian as

$$H = H_{elec} + H_{vib} + H_{rot-hf} + H_{hf} + H_{ext}, \tag{3.1}$$

where H_{vib} is the vibrational Hamiltonian due to the vibration along the internuclear axis and H_{rot-hf} is the rotational Hamiltonian of the molecule including the fine structure, H_{hf} is the hyperfine structure due to the interaction between the nuclear spin of fluorine and the free electron in a certain quantum orbit, and H_{ext} is due to the external fields. As described before, the vibrational and rotational spectra of PbF have been characterized by several groups, and the spectroscopic constants of some other electronic excited states have been further studied by our group[48]. We also measure the hyperfine splitting of the $X_1(^2\Pi_{1/2})(\upsilon = 0)$ and $A(^2\Sigma_{1/2})(\upsilon = 1)$ states for $^{208}Pb^{19}F$, incorporated with the Frosch and Foley's parameters[49]. Based on these parameters, I started to work on the field dependent spectra of $^{208}Pb^{19}F$.

For the $X_1(^2\Pi_{1/2})(\upsilon = 0)$ state of $^{208}Pb^{19}F$, we can express Eq. 3.1 as[43]

$$H = B\mathbf{J}^2 - \Delta\mathbf{S}' \cdot \mathbf{J} + \mathbf{I} \cdot \hat{A} \cdot \mathbf{S}' - D\mathbf{E} \cdot \mathbf{n} + \mu_B \mathbf{B} \cdot \hat{G} \cdot \mathbf{S}'. \tag{3.2}$$

Here I abandon the vibrational band origin constants since the transitions I study will be limited to two vibronic states. Note that there is a significant sign error appearing in the Literatures [43][44]. From Ref.[49] we note the sign difference between the theoretical and experimental results for the hyperfine

constant $A_\perp$. A new basis states of a definite parity has been defined as

$$|FIJM_F p\rangle = \frac{|FIJM_F, \Omega = \frac{1}{2}\rangle + q\chi|FIJM_F, \Omega = -\frac{1}{2}\rangle}{\sqrt{2}}, \tag{3.3}$$

where $\chi = (-1)^F p = \pm 1$, $q = 2(J - F)$ and $p(-1)^{J-\frac{1}{2}} = q\chi$. The evaluation of the matrix elements will be given in Ref. [49], with the eigenenergies expressed as

$$U_{rot} = BJ(J+1) - D_{rot}J^2(J+1)^2 - q\chi\frac{\Delta}{2}(J+\frac{1}{2}), \tag{3.4}$$

$$U_{hf} = \frac{\chi A_\perp}{4} - \frac{q(A_\parallel - \chi A_\perp)}{4(2F+1)} + q\frac{\Delta_{F,\chi}}{2}G(\frac{A_\parallel - \chi A_\perp}{\Delta_{F,\chi}}\sqrt{\frac{F(F+1)}{(2F+1)^2}}). \tag{3.5}$$

Here,

$$G[x] = \sqrt{x^2 - 1} - 1, \tag{3.6}$$

$$\Delta_{F,\chi} = (2F+1)(B - \frac{\Delta}{2}\chi - \frac{1}{2}D_{rot}(2F+1)^2 - \frac{A_\parallel - \chi A_\perp}{2(2F+1)^2}), \tag{3.7}$$

where Δ is the Ω-doubling constant and D_{rot} is the centrifugal distortion constant. All the other parameters have been introduced in Chapter 2. The left side of Fig. 3.2 shows the field-free energy levels with respect to the above formulae. The level structure is exaggerated to be seen more clearly.

An analytical solution of the eigenenergies of the Hamiltonian to the Stark interaction matrix elements cannot be reached, but we can numerically derive the field-dependent energy levels. The simulation of the Stark energy levels of ^{208}Pb^{19}F for the $X_1(^2\Pi_{1/2})(\upsilon = 0)$ and $A(^2\Sigma_{1/2})(\upsilon = 1)$ states are shown in right side of the Fig. 3.2, with F spanning from 0 to 2 and $|M_F| = 0$. In the limit

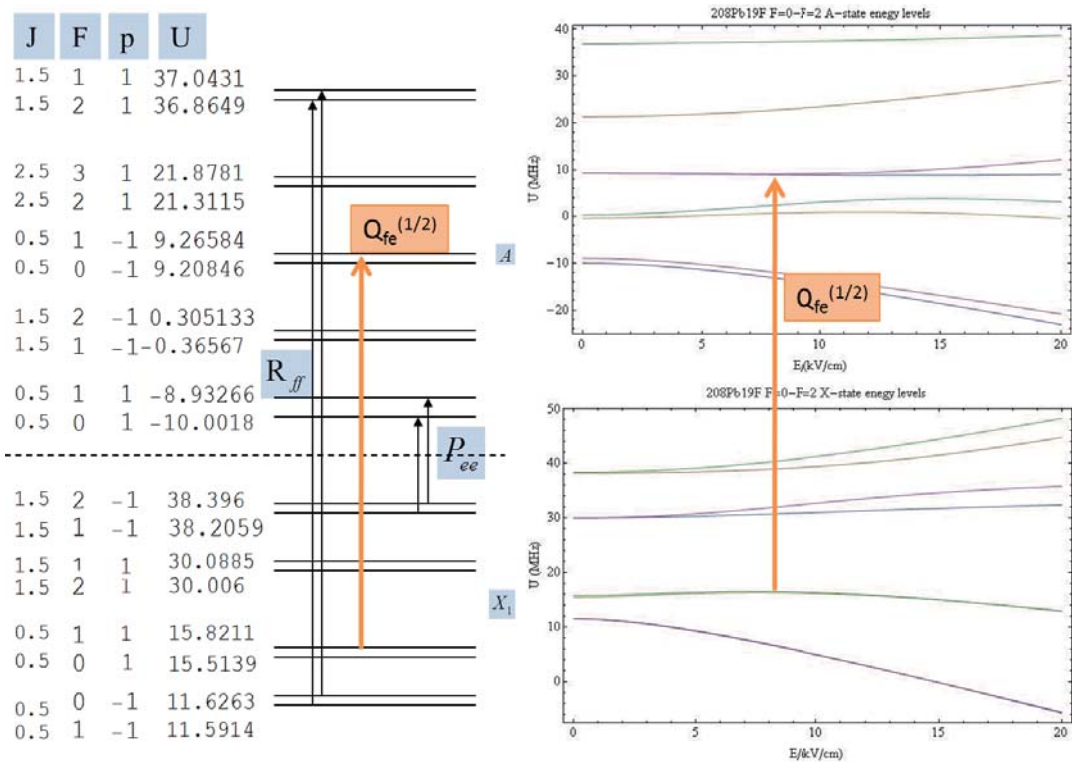

Figure 3.2: Left: Hyperfine level structure of the field-free Hamiltonian for X_1 and A states of $^{208}Pb^{19}F$ with F spanning from 0 to 2(unit is GHz). Here we treat the vibrational band origin energy as 0 for A state for convenience; Right: Field dependent level structure. The $Q_{fe}(1/2)$ transition is the desired e-EDM transition, which will be discussed in Chapter 4.

of a strong field, the Stark shift becomes linear with the applied field, while in the range of the low fields of our measurement (smaller than 2 kV/cm) the Stark dependence is still quadratic. In our experiment, the measurement of the molecular dipole moments are carried out in the weak field limit. The simple quadratic dependent of energy on a weak electric field greatly simplifies our analysis. The polarizability factor of each energy level can be solved numerically by determining the quadratic coefficients. Comparing all polarizability factors I found out that the dipole moment of the X_1 state can be obtained from the

$R_{ff+}[\frac{1}{2}]$ transition(Eq. 3.8), whereas the dipole moment of the A state can be obtained from the $P_{ee+}[\frac{3}{2}]$ transition(Eq. 3.9):

$$X_1(J=\frac{1}{2},F=1,p=-1)\rightarrow A(J=\frac{3}{2},F=2,p=1)(R_{ff+}[\frac{1}{2}]), \tag{3.8}$$

and

$$X_1(J=\frac{3}{2},F=2,p=-1)\rightarrow A(J=\frac{1}{2},F=1,p=1)(P_{ee+}[\frac{3}{2}]), \tag{3.9}$$

where the positive sign means $F=J+1/2$. By implementing all the parameters for the two states, the numerical equations for solving the molecular dipole moments are

$$\Delta U(R_{ff+}[\frac{1}{2}])=[0.53(\frac{D_A}{D})^2+10.35(\frac{D_{X_1}}{D})^2]\times(\frac{E}{kV/cm})^2MHz, \tag{3.10}$$

and

$$\Delta U(P_{ee+}[\frac{3}{2}])=-[7.67(\frac{D_A}{D})^2+0.95(\frac{D_{X_1}}{D})^2]\times(\frac{E}{kV/cm})^2MHz. \tag{3.11}$$

Here, D_{X_1} and D_A represent the molecular dipole moments of $X_1(^2\Pi_{1/2})(\upsilon=0)$ and $A(^2\Sigma_{1/2})(\upsilon=1)$ states, respectively. By carefully choosing the transitions,

we have nearly decoupled the sensitivity of the molecular dipole moment to the ground state (Eq.3.10) from that to the excited state (Eq.3.11). This greatly increases the accuracy for both of the dipole measurements.

3.3 Experiment

In our experiment, a variant technique of Resonance-Enhanced Muti-Photon Ionization(REMPI) called pseudo-continuous REMPI(pc-REMPI) is employed. Traditional REMPI techniques typically utilizes mostly tunable lasers operating at a repetition rate at about 10-5000 Hz. For our previous 10 Hz, 10 ns Nd: YAG pumped dye laser systems, its 10 Hz repetition rate gives rise to the low effective duty cycle with respect to different transition states[50]. The new pseudo-continuous mode-locked neodymium doped yttrium vanadate (Nd:YVO_4) laser (HighQLaser, picoTrain) produces a 6 ps pulse width at 476 nm with an output power of 800 mW and a repetition rate of 76 MHz. It not only provides higher average power and peak power than the pulsed dye laser that we used previously, but raises the effective duty cycle to near unity. The duty cycle is defined as the ratio of the lifetime of the excited state after the continuous-wave laser and the repetition rate of the pulsed laser. Additionally, the pico-second laser ionizes the D state with an appreciable lifetime compare with the 6 ps pulse width[50].

The experimental setup is similar to those appearing in the Ref. [49]. The experimental setup can be treated into two separated regions: Pb^+/e^-

pair creation and detection. A PbF supersonic beam is created by heating lead in a MgF_2 nozzle to around 1000°C. Carried with high-pressure Helium carrier gas, the supersonic molecular beam flux is then fed into the detection region. The beam in the detection region is shined with two lasers focusing tightly in the center of detection region. The diode laser (Toptica DL-100, 436 nm, 7 mW) drives the $X_1(\upsilon = 0) \rightarrow A(\upsilon = 1)$ transition and the 476 nm radiation with averaged power of about 800 mW and 6 ps pulse width drives the $A(\upsilon = 1) \rightarrow D(\upsilon = 0) \rightarrow PbF^+$ transition. Part of the 436 nm radiation is introduced into an etalon (1 GHz free spectral range, Toptica, FPI 100) stabilized by a Zeeman stabilized HeNe laser (MicroG LeCoste, ML-1). The etalon will provide frequency signatures of the 436 nm radiation, either by grating scan of the diode or the pressure tuning[49]. The function of the etalon in our experiment will be further discussed in Appendix A. To create the 476 nm radiation, we use a mode-locked Nd:YVO_4 laser to produce 3.8 watts of 532 nm radiation and 3.6 watts of 1064 nm radiation. The 532-nm radiation then enters the optical parametric oscillator (OPO, Angewandte Physik und Elektronik Levante Emerald) to produce about 1.3 watts radiation of 864 nm. The 1.3 watts of 864 nm radiation and the 3.6 watts of 1064 nm radiation , which is optically delayed to match maximum overlap of the pulses, are combined in a sum-frequency generation crystal LBO (Lithium Triborate crystal, Red Optronics) to produce up to 800 mW of 476 nm laser radiation. With 436 nm radiation cylindrically focused along the direction of the supersonic molecular

PbF beam, and 476 nm radiation spherically focused tightly, the PbF^+/e^- pair are created. Both of the laser radiations are focused in an overlapped way such that a substantial focal volume will produce a significant mount of PbF^+/e^- pairs.

The other region is the detection region. The photo-ion and photo-electron pair are then seated in the time-of-flight coincidence detector[51]. In general, the detector can be divided into four regions: extraction region, time-of-flight region, charge amplification (microchannel) plates(MCPs), and a charge-to-voltage transducer. The photo-ion and photo-electron pair are accelerated into two opposite directions in the extraction region, and then enter the time-of-flight region where net zero electric fields are applied on both sides. The whole extraction region and each of the two time-of-flight region are designed in such a way that both the mass discrimination and signal count rates are optimized[51]. One interesting feature of the design, which is also necessary for this experiment, is the independence of the incident energy on the MCPs from the variation of the extraction field. We can have different extraction fields to apply Stark shifts on the desired energy levels, while the sensitivities of the MCPs are unchanged due to the same impact energies on them. After the Pb^+/e^- impacts on the front surface of the MCP, a cloud of electrons will be generated and collected by the charge-to-voltage transducer to create a Start/Stop pulse in a timing amplifier (Ortec model 9327). Both the time delay and the time of the start pulse are logged by the multi-channel scaler (Ortec model 9353), whose internal clock is

synchronized to the diode laser sweeping sync signals. The whole experiment setup can be illustrated as Fig.3.3.

3.4 Analysis

The frequency dependent Stark shifts are obtained for an extraction electric field 1000V, 500V and 300V, separately. The two extraction plates are spaced by 2.54 cm, and the electric fields are 0.787 kV/cm, 0.393 kV/cm and 0.236 kV/cm. Fig.3.4 shows the two field-dependent transitions $R_{ff}(\frac{1}{2})$ and $P_{ee}(\frac{3}{2})$.

There are a few things I need to address about these data. First, the data

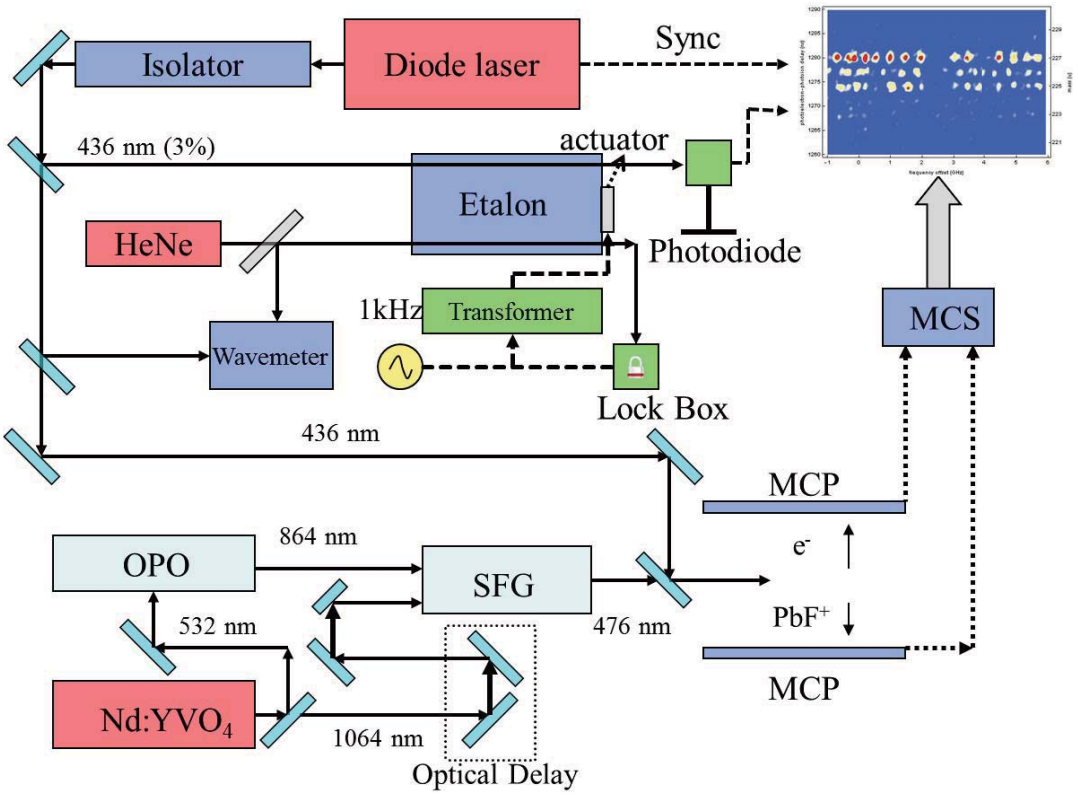

Figure 3.3: Experimental setup for spectroscopic measurement of $^{208}Pb^{19}F$ molecule. This is a similar experimental setup in Ref.[49].

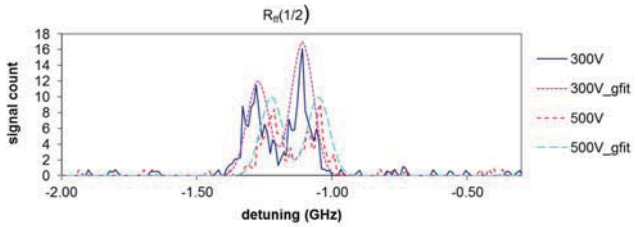

(a) Field-dependent $R_{ff}(\frac{1}{2})$ transition

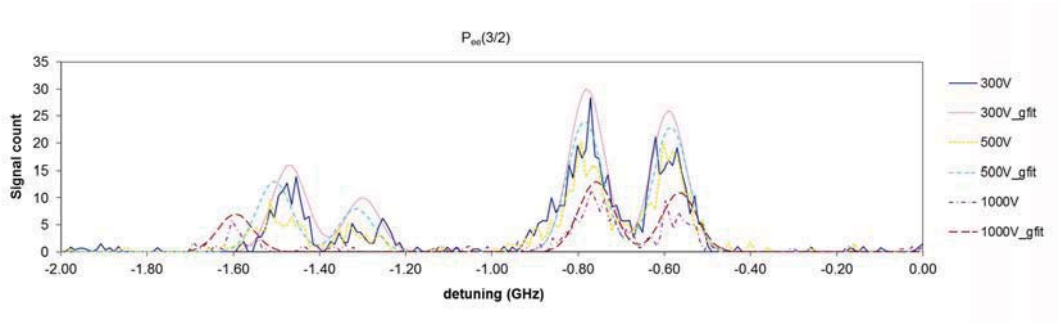

(b) Field-dependent $P_{ee}(\frac{3}{2})$ transition

Figure 3.4: Field-dependent $X_1 \rightarrow$A transitions of $^{208}Pb^{19}F$, with E=0.236 kV/cm, 0.393 kV/cm and 0.787 kV/cm, separately. The frequency detuning center for $R_{ff}(\frac{1}{2})$ transition is 686,484 GHz. For $P_{ee}(\frac{3}{2})$ it is 686,391 GHz.

has a limited statistics imperfectly. The statistics can be dramatically increased by taking a much longer time in data-taking. Unfortunately, the diode laser (Toptica DL100) only allows for around 15 minutes of data collection before it mode-hops. Meanwhile, the diode laser light path makes a long detoured way to the chamber, with two optical tables and one chamber table, so the tight-focused alignment will be disturbed easily and contribute to the decreasing count rate. One can offset these experimental difficulties by applying a larger extraction field. Ideally, it can increase the energy splitting, thus increasing the sensitivity to the dipole moment measurements. But a larger extraction field will obscure the mass discrimination and make the transitions of each isotope

	This work (66% C.L.)(Debye)	Ref.[24](Debye)	Ref.[52](Debye)
D_{X_1}	3.5 ± 0.3	4.62	4.26
D_A	2.8 ± 0.2	5.5	2.51

Table 3.2: Molecular dipole moments of X_1 and A states of $^{208}Pb^{19}F$, in comparison with the results from other work.(N.B. 1 Debye =0.3934 a.u.)

interfere with each other. For both transitions, the maximum field and count rate have been optimized against these competing experimental factors. By fitting the data to a peak-finding program, we obtained a spectral linewidth around 90 MHz. Since the diode laser is cylindrically focused into the ionizing region, the ionizing region and the $X_1 \rightarrow A$ transition region will not necessary to be the same location due to the supersonically-moving molecules. Therefore, the pseudo-continuous laser pulses contribute little to this spectral linewidth, however, the natural linewidth of A state, the divergence of diode laser into the excitation region, and the speed of the molecular beam greatly restrict the spectral resolution.

By putting the Stark shifts and related electric fields into the numerical solutions Eq. 3.10 and Eq. 3.11, we can derive the molecular dipole moments for $X_1(^2\Pi_{1/2})(\upsilon = 0)$ and $A(^2\Sigma_{1/2})(\upsilon = 1)$ states, which are shown in Table 3.2

Here, the reported value of D_A is different of the preliminary value 5.5±0.2 Debye in Ref. [49]. In Ref. [49], the author used the theoretically predicted D_{X_1} from Ref. [24], to obtain D_A from the experimental data. The result matches very well with the theoretically predicted D_A in Ref. [24], but disagrees with

a recently published paper Ref. [52]. Our experimental results show a better agreement with Ref. [52], which has a corrected analytical form of the energy level structure. I will cover more about this corrected analytical form in Chapter 5.

3.5 Conclusion

In this chapter we demonstrated the molecular dipole moments of $X_1(^2\Pi_{1/2})(\upsilon = 0)$ and $A(^2\Sigma_{1/2})(\upsilon = 1)$ can be achieved by analyzing the Stark spectroscopy of $X_1 \rightarrow$A transition of $^{208}Pb^{19}F$, using the pc-REMPI detection scheme. Starting from the theoretical evaluation of the matrix elements of the molecular Hamiltonian, we studied the field-dependent energy splittings, and found two field-sensitive transitions which are used for the calculation of the molecular dipole moments. Our results are in a reasonable agreement with the recently published results in Ref. [52]. However, as I addressed above, there are still more improvements which can be achieved. A tunable, frequency-doubled, high power diode laser, integrated by excellent thermal and mechanical mechanism, will probe the desired transition at a higher count rate, better spectral resolution, and allow us to substantially improve our measurement of D_{X_1} and D_A.

Chapter 4

Design of Biased Stark Guides for Polar Molecules

In this chapter, I will talk about the three possible uses of the biased Stark guides in our e-EDM measurement. The design of these guides is motivated by their possible use in a precision measurement of the electron's electric dipole moment. These guides may also have applications in the alignment-preserving transportation of ultracold molecules. Then I will give a simple schematic explaining the optical double resonance e-EDM experiment using a 10-meter long guide. The statistical uncertainty based on this beam machine will be analyzed in the end.

4.1 Introduction

In general, the elementary particles' EDM searches can be divided into three major categories[7]. Many competitive groups use paramagnetic atoms or molecules as the probe for the e-EDM(Tab. 1.3). The recent result reported by Hinds' group set a limit on the e-EDM as $|d_e| < 1.05 \times 10^{-27} e{\cdot}\text{cm}$, with 90% confidence[10]. The result, as we can see from Hinds' paper, depends mostly on the statistical sensitivity. The statistical sensitivity, however, depends on some parameters that are common to most of the atomic or molecular e-EDM searches[53]. From Hind's paper, the statistical uncertainty of e-EDM for polar

molecules is

$$\delta d_e = \frac{\hbar}{2\tau E_{eff}\sqrt{T(dN/dt)}}, \tag{4.1}$$

where τ is the coherence time, E_{eff} is the effective internal electric field (in orders of GV/cm), T is the total measurement time and dN/dt is the count rate. Therefore, we can reduce the statistical uncertainty by increasing the coherence time, enhancing the internal effective field or/and increase the count rate. In our molecular beam experiment, the coherence time is the time of flight through the electric field region[53], and is about 1 ms in our experiment. In our optical double resonance measurement system, the biased Stark guide is implemented to enhance the coherence time by several orders of magnitude.

4.2 Theory

The following part of this chapter is as it appears in the recently published paper by Tao Yang, James Coker, J. E. Furneaux, and N. E. Shafer-Ray, *Designs of biased Stark guides for polar molecules* in *Physics Review A 85, 063403, 2007.*

The Stark-guided e-EDM experiments envisioned here are shown schematically in Fig. 4.1. In brief, a beam of polar molecules is polarized in a region of uniform electric field using optical and/or microwave radiation. This polarization process creates a coherent superposition of states that differ only by the sign of the projection M_F of the total angular momentum of the molecule onto an electric field axis. The molecules are then allowed to evolve for a time τ in the electric field of a long Stark guide. This guide is biased to have a minimum value of the electric field that is strong enough to align

the dipole moment of the molecule with respect to the electric field. After polarization and guiding, the molecules enter a second region of uniform electric field and are probed with optical/microwave radiation to determine the accumulated quantum phase between the two states. For a properly designed experiment, reversal of the electric field in the system will result in a difference in phase that is proportional to the e-EDM. In the language of beam resonance experiments, the biased Stark guide becomes the Ramsey cavity. By guiding the particles tens or even hundreds of meters, the coherence time of the experiment (and hence the sensitivity to an e-EDM) can be enhanced by several orders of magnitude. For the purpose

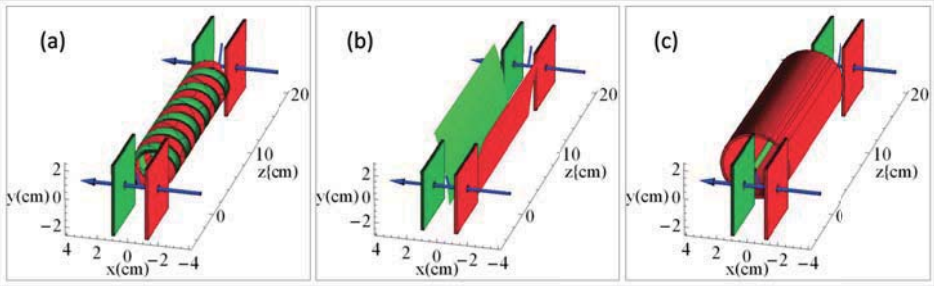

Figure 4.1: (Color online) Two uniform field regions connected by various guides. In the envisioned experiment, a beam of molecules is polarized by laser radiation, guided by the field within the electrodes, and then probed with laser radiation. The guides shown are only 15 cm long, but guides exceeding 100 meters may be considered.

of preventing the low-field seeking states to become degenerate with high-field seeking states through nonadiabatic transitions, we must avoid field regions with zero electric field[54]. However, two-dimensional potentials have a minimum in the magnitude of electric field at a location in space at which the electric field vanishes. This fact is not by any special design. Rather it is a result of a theorem conceived and proven by Samuel Meek[55]. This theorem starts with Maxwell's equations in a vacuum to prove that, in the two dimensional case, a local minimum of E^2 cannot occur at a point where $\vec{E} \neq 0$. This result presents a problem for both the e-EDM measurement we envision and for any application of a Stark guide for which one wishes to guide polar molecules while conserving the M state alignment of the system. Next we present three possible ways one might still guide a beam of molecules over long distances in a biased electrostatic guide.

4.2.1 Case 1: The helical guide.

As stated in the introduction, we are interested in creating a Stark guide of molecules for which the minimum electric field magnitude is non-zero. For this reason, a purely two dimensional guide, such as a modified hexapole or quadrupole guide is inappropriate: By Meek's theorem, the minimum electric field magnitude in such a guide will occur at a point in space for which $\vec{E} = \vec{0}$.

The first possible solution to this problem we present in this section is a *helical Stark guide* that employs curved plates spiraling around a central guide region in order to guide molecules in the z direction (Fig. 4.1.a). When opposite voltages $\pm V$ are applied to the two electrodes of the guide, the potential

$$\Phi = -E_o \frac{2I_1(kr)}{k} \cos(kz - \phi) \tag{4.2}$$

is created. Here I_1 is the modified Bessel function of the first kind and $k = 2\pi/\lambda$ is a parameter that determines the pitch of the helix. Along the axis of this guide, the electric field is of constant magnitude E_o and rotates with the z dimension

$$\vec{E}(\vec{r} = \vec{0}) = E_o(\cos kz\hat{\imath} + \sin kz\hat{\jmath}). \tag{4.3}$$

The electric field magnitude E throughout the guide can be shown to be given by

$$\begin{aligned} E = E_o\{&[1 + (kr)^2 f_p(kr)]^2 \cos^2(kz - \phi) \\ &+ [1 + (kr)^2][1 + (kr)^2 f_a(kr)]^2 \sin^2(kz - \phi)\}^{\frac{1}{2}}. \end{aligned} \tag{4.4}$$

Here we have defined the two even functions $f_a(\alpha)$ and $f_p(\alpha)$:

$$f_a(\alpha) = \frac{2}{\alpha^3} I_1(\alpha) - \frac{1}{\alpha^2} = \sum_{n=0}^{\infty} \frac{1}{4(n+1)!(n+2)!} (\frac{\alpha}{2})^{2n}, \tag{4.5}$$

$$f_p(\alpha) = \frac{2}{\alpha^2} \frac{dI_1(\alpha)}{d\alpha} - \frac{1}{\alpha^2} = \sum_{n=0}^{\infty} \frac{2n+3}{4(n+1)!(n+2)!} (\frac{\alpha}{2})^{2n}. \tag{4.6}$$

We note that $f_a(0) = 1/8$, $f_p(0) = 3/8$, and both functions increase rapidly as α goes from zero to positive infinity. Thus the minimum field magnitude everywhere in the twisted guide is E_o, with the field rapidly increasing as a function of distance from the center of the guide.

The electrodes of the helical Stark guide shown in Fig. 4.1.a are equipotential surfaces of the potential given by Eq. 4.2. The topology of these surfaces suggests that the guide could easily be made from

two intertwined wires twisted with a pitch-length $\lambda = 2\pi/k$ to inner-diameter d ratio determined by the voltage $\pm V_o$ on the electrodes:

$$\frac{1}{\pi} I_1(\pi \frac{d}{\lambda}) = \frac{V_o}{\lambda E_o}. \tag{4.7}$$

A numerical solution to this transcendental equation is given in Fig. 4.2.

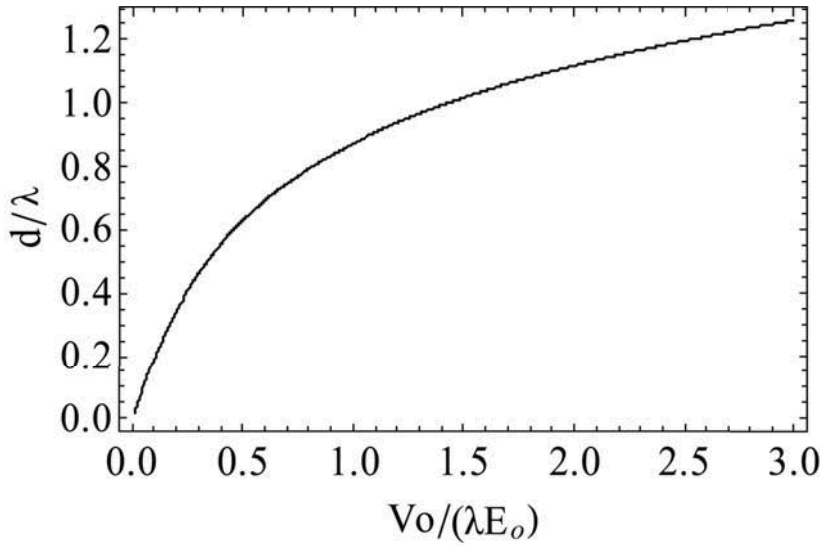

Figure 4.2: Relationship between the d/λ and the $V_o/(\lambda E_o)$ for the helical guide. Here voltages $\pm V_o$ are placed on the electrodes, d is the inner diameter of the guide, $\lambda = 2\pi/k$ is the pitch length, and E_o is the bias field of the guide.

To test the performance of the helical guide, we performed classical trajectory calculations. Here we assume a force given by

$$\vec{F} = -\frac{\partial U(E)}{\partial E} \vec{\nabla} E + m\vec{g}, \tag{4.8}$$

where $U(E)$ is the Stark potential of the guided state, m the mass of the particle, and $\vec{g}$ the acceleration due to gravity. For illustrative purposes we assume $U(E)$ is that of the $J = 1/2$, $F = 1, |M_F| = 1$, Ω_+ rotational state of the $X_1(v = 0)$ ground state of the e-EDM sensitive ^{208}Pb^{19}F molecule. The Stark energy is determined by diagonalizing a spin-rotational Hamiltonian determined from detailed microwave and optical spectroscopy[22]. We have carried out this analysis and fit this potential to a quadratic polynomial

with the result

$$U(E) = [23.056(\frac{E}{10\text{kV/cm}})^2 - 31.358(\frac{E}{10\text{ kV/cm}})^3 + 10.004(\frac{E}{10\text{kV/cm}})^4]\mu\text{eV}, \tag{4.9}$$

where the fit is valid in the range $0 < E < 10$ kV/cm. A plot of this potential is given in Fig. 4.3.

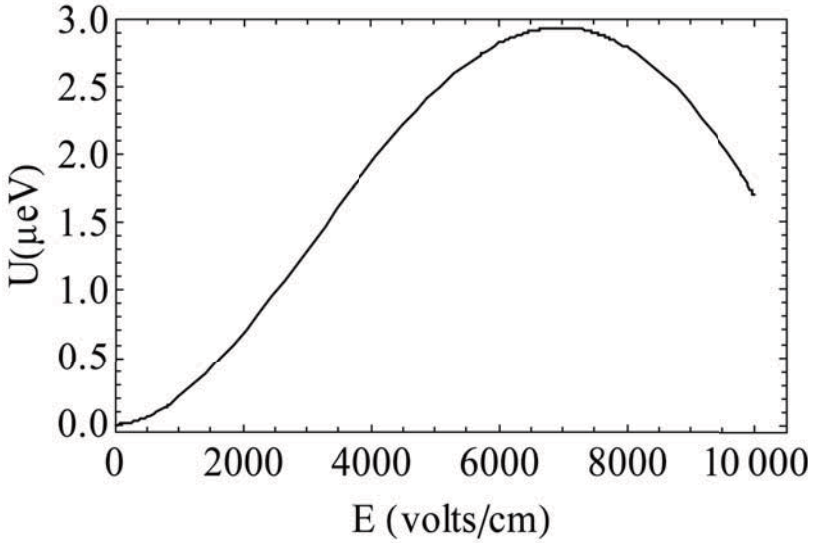

Figure 4.3: Stark energy of the low-field seeking $X_1\ ^2\Pi_{1/2}(v = 0,\ F = 1,\ |M_F| = 1,\ J = 1/2,\ \Omega_+)$ state of $^{208}Pb^{19}F$.

Fig. 4.4.a gives the transverse $(x - y)$ trajectory of a typical molecule with the Stark potential of Eq. 4.9 as it travels a distance $z = 10,000$ cm down a helical guide with $\lambda = 2\pi/k = 2.5$ cm. This electric field is chosen in such a way that it won't extend to the high field range to become high-field seeking, and it also needs to be large enough to fully polarize the PbF molecules. From Fig. 4.3, we can therefore choose a moderate field $E_o = 5$ kV/cm, which is subject to the experimental test. The initial conditions of this trajectory are given by $\vec{r} = (0.10\ \hat{\imath} - 0.09\ \hat{\jmath} + 0.00\ \hat{k})$ cm and $\vec{v} = (-6.5\ \hat{\imath} - 46.2\ \hat{\jmath} + 20,000\ \hat{k})$ cm/s. It is notable that the molecules are guided 10,000 cm (4000 twists) without being lost. It is not immediately obvious that this three dimensional guide will lead to stable trajectories as the energy in axial motion could, in principle, be coupled to the transverse motion. For the guide shown and a beam velocity of 200 m/s, particles with a transverse-kinetic

plus potential energy less than or equal to 85% of the barrier height of 2.94 μeV were guided the entire 100 m length of the guide. This corresponds to an acceptance of approximately 2×10^{-5} sr.

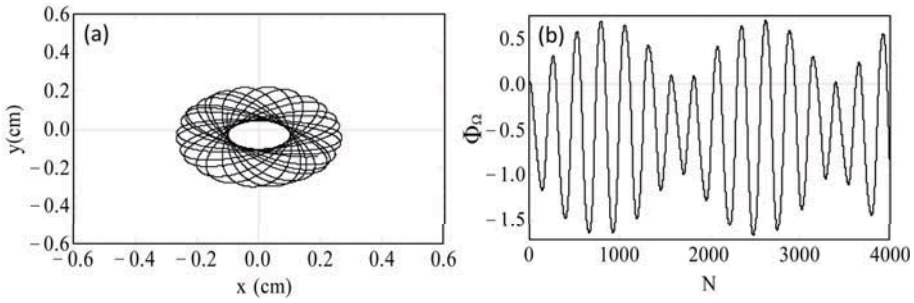

Figure 4.4: (a) Simulated x-y trajectory of a particle as it moves $N = 4000$ $twists = 100$ m through the helical guide described in the text. (b) Accumulated geometric phase after a particle with the initial conditions described in the text travels from a uniform field region, through a helical guide of N turns, and exits into a second region of uniform field region.

Although the helical guide is effective at guiding polar molecules over long distances, it is not likely to be suited to an e-EDM measurement. Whereas the helical guide will conserve the $|M_F|$ state population, it can not be expected to conserve any phase coherence between two states that differ only by the sign of M_F. This is because, as the electric field direction is allowed to vary in three dimensions, a geometric phase ϕ_Ω is accumulated which leads to rapid decoherence of the molecules in the beam. To quantify this geometric phase effect, we imagine an experiment in which molecules are polarized in a uniform electric field, travel the length of a helical guide, and finally are probed with laser radiation(Fig. 4.1). The expected rate of molecular detection is expected to be given by

$$\Gamma = \Gamma_N \left(\frac{2-c}{2} - \frac{c}{2} \cos[2(\phi_{EDM} + \phi_B + \phi_D + \phi_\Omega)] \right). \qquad (4.10)$$

Here Γ_N is the rate of detection of an unpolarized beam of molecules and c is an experimentally determined contrast with $0 < c < 1$. The angle $\phi_{EDM} = d_e E_{eff} \tau / \hbar$ is the effect of the e-EDM with d_e the electric dipole moment of the electron, τ the time of flight of the molecule as it travels from the polarization region to the probe region, and E_{eff} the effective internal field of the molecule. For heavy diatomic radicals, E_{eff} is of the order of 10 to 100 GV/cm[25]. The angle $\phi_B = g \mu_B \tau / \hbar$ is the contribution of background magnetic

fields. For the purpose of this discussion, we assume that magnetic fields are shielded so ϕ_B is insignificantly small. The angle ϕ_Ω is due to the geometric phase effect. Lastly, ϕ_D is the angle between the initial and final laser polarizations and is modulated to gain sensitivity to $\phi_{EDM} + \phi_\Omega$. Final determination of the e-EDM would be determined by a reversal of the electric field which would change the sign of ϕ_{EDM}, but not ϕ_Ω.

In the adiabatic approximation, the phase ϕ_Ω may predicted by performing the integration

$$\phi_\Omega = \int -\frac{2|M_F|}{e^2}\left(\frac{d\vec{e}}{dt} \times \vec{e}\right) \cdot \hat{z}\ dt \tag{4.11}$$

over the trajectory[58]. Here $\vec{e} = \hat{E} + \hat{z}$ where $\hat{E}$ is the direction of the electric field and $\hat{z}$ is the direction of a laboratory-fixed quantization axis, which we take to be along the axis of the guide. A plot of ϕ_Ω modulus 2π verses N is given for the trajectory of Fig. 4.4.b. Here N is the number of twists of the helical guide and the total guide length is (2.5 cm) $\times N$. The large-amplitude oscillations in this phase as a function of distance down the guide is very sensitive to the initial conditions of the trajectory and hence very difficult to control. For this reason, the almost random final geometric phase of each molecule will to lead to rapid decoherence of the experimental measurement and, as a result, loss of sensitivity to the e-EDM.

Although the helical guide is most likely not of use to an e-EDM experiment, it might be of use in other applications which require the transport of molecules from one region of space to another without loss due to mixing of $|M_F|$ states. We also note that the combined rotating radial field and oscillating axial field seen by a polar molecule is similar to the field seen by a trapped ion in an envisioned e-EDM experiment. However, in the case of this ion trap experiment, the axial field is orders of magnitude smaller than the radial field and, and as a result, the geometric phase is not a major concern[59].

4.2.2 Case 2: The Stark Gravitational Guide

Here we show that Meek's theorem can be overcome by creating a *Stark gravitational guide* that uses two slightly distorted field plates (see Fig. 4.1.b). This distortion leads to an increasing Stark energy when a polar molecule moves in the down $(-\hat{y})$, left $(-\hat{x})$, or right $(+\hat{x})$ direction. The fact that the Stark energy decreases as the molecule moves in the up $(+\hat{y})$ direction assures compliance with Meek's theorem. However, this decrease is not enough to overcome

gravity. Thus, in this manner, one constructs a trough for molecular flow without dispersion. The distorted plates of Fig. 4.1.b are equipotential surfaces of the following electric potential, created from a series of increasingly high order terms odd in x, each with zero Laplacian:

$$\Phi = -E_o x + \beta_1\, xy + \beta_3(xy^2 - \frac{1}{3}x^3) + \beta_5(x^3y^2 - \frac{1}{2}xy^4 - \frac{1}{10}x^5). \quad (4.12)$$

The Stark gravitational potential is given by

$$U_{sg}(x,y) = mgy + U_i(E). \quad (4.13)$$

Here $\vec{E} = -\vec{\nabla}\Phi$, and mg is the weight of the molecule. For the purpose of example, we continue with the example system of the last section, namely, the Stark energy $U_i(E)$ of the $X_1\ ^2\Pi_{1/2}$ $(v = 0, F = 1, |M_F| = 1, J = 1/2, \Omega_+)$ state of $^{208}Pb^{19}F$. Rewriting Eq. 4.9 as

$$U_i(E) = C_2E^2 + C_3E^3 + C_4E^4, \quad (4.14)$$

$U_{sg}(x,y)$ can be written in terms of a series expansion in x and y. The potential parameters β_1, β_3, and β_5 may be taken to zero in the terms of order y, x^2y, and x^4y. The result is the Stark gravitational potential of the form

$$U_{sg}(x,y) = U_i(E_o) + \frac{1}{2}k_x x^2 + \frac{1}{2}k_y y^2 + O[y^3] + O[x^4], \quad (4.15)$$

with

$$\begin{aligned} k_x &= \frac{(mg)^2}{2C_2E_o^2 - 4C_4E_o^4} \\ &= 0.0195\ \mu\text{eV/cm}^2 = 23.4\mu\text{K/cm}^2, \quad (4.16) \\ k_y &= \left[\frac{4C_2^2 + 6C_2C_3E_o - 9C_3^2E_o^2 - 60C_3C_4E_o^3 - 80C_4^2E_o^4}{(2C_2 + 3C_3E_o + 4C_4E_o^2)^2}\right] k_x \\ &= 0.0233\ \mu\text{eV/cm}^2 = 28.0\mu\text{K/cm}^2. \quad (4.17) \end{aligned}$$

Here the values of k_x and k_y are taken by assuming coefficients C_i that model the $J = 1/2$, Ω_+, $F = 1, |M_F| = 1$ quantum state of interest in this experiment and a trap field bias field $E_o = 2500$ V/cm. The simple harmonic potential described by the k_x and k_y terms alone does a very good job of modeling the exact Stark gravitational potential $U_{sg}(x,y)$ everywhere inside a guide created by plates separated by 2 cm.

Two factors make the Stark gravitational guide somewhat miserable to work with. The first is that the trap force parameters

(constants k_x and k_y) rapidly decrease with increasing value of E_o, making a central field much greater than 2500 V/cm impossible. This limits the polarization field, and hence e-EDM sensitivity of the state of the PbF molecule we considered in the last section to 8.2 mHz/($10^{-27}e$ cm), roughly 65% of its sensitivity when fully polarized. A second is the fact that the trap depth is frustratingly small, stopping only those particles that begin their journey from the center of the trap with a transverse velocity of 9 cm/s or less. For a beam velocity of 200 m/s, this corresponds to an acceptance of only 6×10^{-7} sr. However, the guide has an overwhelmingly positive feature that may make its disadvantages worth coping with: Because the trap is two-dimensional, there is no accumulation of the geometric phase as a polarized molecule travels down the beam. This implies the length of the guide is limited only by one's ability to control the vacuum, black-body radiation, and background magnetic fields. Indeed, one can imagine an 1 km machine with 5 s coherence time that fits within one's abilities to control these factors.

4.2.3 Case 3: The Cylindrical Guide

The guides of the previous sections collimate a beam of low-field seeking states. Here we consider a guide of high field seeking states. Because it is not possible to create a local maximum in the magnitude of an electric field, this guide must be a dynamic guide for which the translational angular momentum of the molecules keeps them from colliding into a central electrode. The electrodes of this guide (Fig.

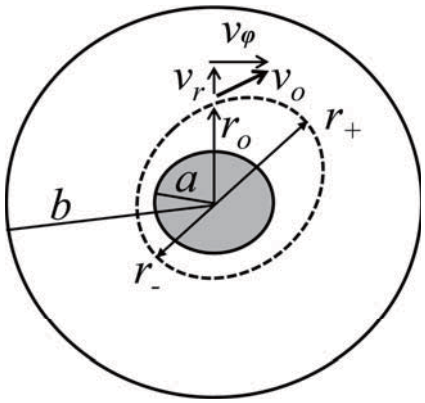

Figure 4.5: Cross section of the cylindrical guide.

4.1.c and Fig. 4.5) are a central rod of radius $a = 0.2$ cm surrounded by a coaxial cylindrical electrode of inner radius $b = 1.0$ cm. For the case that voltages $V = \pm 8050$ V are applied to the electrodes, the field magnitude varies inversely with r from $50,000$ V/cm to

10,000 V/cm. The strong electric field strength can not only keep the molecular beam of the high-field seeking state from diverging, but also fully polarize the PbF molecule to gain enough sensitivity to the e-EDM measurement. This field strength is manageable in the laboratory environment, but the determination of the appropriate values is still dependent on the design of the electrodes and the ability of controlling the vacuum. For the case of a molecule interacting with a linear Stark interaction $U_S = -\bar{d}\,E$, the energy of a molecule in the guide is (ignoring gravity) that of Kepler motion:

$$\frac{U}{m} = -\frac{k}{r} + \frac{1}{2}v^2, \tag{4.18}$$

with

$$k = \frac{\Delta V}{\ln(b/a)m}\bar{d}. \tag{4.19}$$

Here $\Delta V = 16100$ V is the potential difference between the electrodes and m the mass of the molecule. For strongly mixed $J = 1/2$, $J = 3/2$ states of a $^2\Sigma_{1/2}$ or $^2\Pi_{1/2}$ molecule, the approximation $\bar{d} \approx \frac{2}{3}d$, where d is the dipole moment of the ground state of the molecule, may be used. Over the range of fields in the cylindrical guide described here, this value of $\bar{d}$ does a good job modeling the Stark interaction of the e-EDM sensitive low field seeking states of YbF($d = 3.58$ Debye[60]), PbF($d = 3.40$ Debye[22]), and HgF($d = 2.18$ Debye[24]).

We now consider the fraction of a beam of molecules entering the guide a distance r_o away from the center that will be sent into orbits that do touch the electrodes (*i.e.*, for which $a < r_-$ and $b > r_+$, in Fig. 4.5). We make approximation of Keplerian motion to allow us to proceed analytically. Because of the dispersion of beam velocities, we expect each molecule to enter with a unique initial transverse velocity $\vec{v}_o = v_r\hat{r} + v_\phi\hat{\phi}$ as shown in Fig. 4.5. If a molecule enters with $v_r = 0$ and $v_o = v_c = \sqrt{k/r_o}$, then the molecule will enter a circular

analyzing other Kepler orbits, one finds the range of input velocities that will lead to stable trajectories:

$$v_c\sqrt{\frac{2a}{r_o + a}} < v_\phi < v_c\sqrt{\frac{2ab}{(a+b)r_o}} \tag{4.20}$$

and

$$|v_r| \leq \sqrt{\frac{2(r_o - a)}{a}\left(\frac{r_o + a}{2a}v_\phi^2 - v_c^2\right)} \tag{4.21}$$

or

$$v_c\sqrt{\frac{2ab}{(a+b)r_o}} < v_\phi < v_c\sqrt{\frac{2b}{r_o+b}} \tag{4.22}$$

and

$$|v_r| \leq \sqrt{\frac{2(b-r_o)}{b}\left(v_c^2 - \frac{r_o+b}{2b}v_\phi^2\right)} \tag{4.23}$$

This region of velocity space for the case that $r_o = (a+b)/2 = 0.6$ cm, is given in Fig. 4.6 for the molecules ^{174}Yb^{19}F, ^{208}Pb^{19}F, and ^{198}Hg^{19}F.

To test the approximations that, for the case of ^{208}Pb^{19}F, gravity can be ignored and $U \approx -\frac{2}{3}dE$, we carried out a Monte Carlo calculation. This calculation incorporates both gravity and a potential energy $U(E)$ taken from a detailed calculation of the Stark interaction using known spectroscopic parameters of the high-field seeking $X_1(v=0,\ F=1,\ |M_F|=1, J=\frac{1}{2},\ \Omega_-)$ state of ^{208}Pb^{19}F. In this study, values of v_ϕ and v_r are chosen randomly and trajectories are evolved from the point $x=0$, $y=0.6$ cm. For each trajectory that evolves for 50 ms, the initial velocities v_ϕ and v_r are recorded and plotted on Fig. 4.6. From this calculation we see that the Kepler approximation slightly overestimates the acceptance of the guide.

Like the Stark gravitational guide, the electric field in this guide is constrained to two dimensions and, as a result, the geometric phase effect is not expected to be of concern. This guide has many advantages over the Stark gravitational guide. One is that, for $^2\Sigma_{1/2}$ states with small spin rotational constants, the high field seeking ground state is more sensitive to an e-EDM than low field seeking ground states. For example, the most sensitive low-field seeking state of ^{174}Yb^{19}F, is four to five times less sensitive to an e-EDM than is the most sensitive high-field seeking state. For ^{198}Hg^{19}F this low-field seeking state is approximately 2 times less sensitive. In addition, while both the low- and high- field seeking states of the ground $^2\Pi_{1/2}$ state of ^{208}Pb^{19}F exhibit similar sensitivities to an e-EDM, the Stark gravitational guide only functions at low fields for which the PbF molecule is only partially polarized, leading to an approximately 35% reduction in sensitivity. Thus for each of these three important e-EDM molecules, sensitivity to an e-EDM is substantially greater in the cylindrical guide.

A second advantage of the cylindrical guide is its tremendous acceptance. This acceptance is given by the area of the region of trapped velocities divided by the beam velocity squared. For a cylindrical guide of a 200 m/s beam of PbF , this acceptance is 3×10^{-4} sr, a factor of 500 times greater than the 6×10^{-7} sr acceptance of the Stark gravitational guide. For a statistics limited

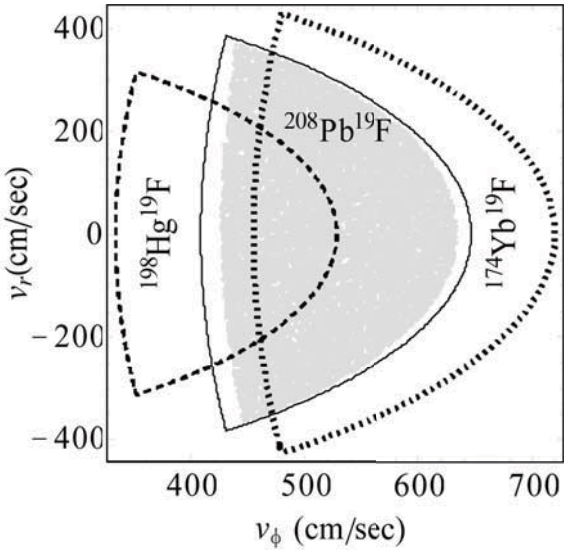

Figure 4.6: Kepler-motion prediction of acceptance velocities of the cylindrical guide for the ground state of ^{198}Hg^{19}F (dashed line), ^{208}Pb^{19}F(solid line), and ^{174}Yb^{19}F(dotted line.) The shaded area indicates initial conditions of stable trajectories in a Monte Carlo Simulation assuming motion of high-field seeking ground-state ^{208}Pb^{19}F($v = 0,\ F = 1,\ |M_F| = 1,\ J = \frac{1}{2},\ \Omega_-$) molecules governed by Eq. 4.8 and a potential energy $U(E)$ taken from a detailed calculation of the Stark interaction using known spectroscopic parameters.

experiment, this increased acceptance could, in principle, lead to a factor of 20 improvement in sensitivity to an e-EDM. Many factors may offset this advantage. One problem with the cylindrical guide is that the electric field at the entrance and exit is complex and likely to cause a substantial spatially-dependent geometric phase shift that restricts the probe region to a small volume in space. A second problem is the beam must be loaded with a substantial translational angular momentum. This angular momentum may couple with distortions in the electric field to create false e-EDM signals. If these problems can be overcome, then the cylindrical guide may prove to be the most promising candidate for use as a Ramsey cavity in an e-EDM experiment.

4.3 Summary of the Three Guides

We have introduced three guides of polar molecules for possible use as the Ramsey cavity in an optical double resonance measurement of the electron's electric dipole moment (e-EDM). Each of these guides

must overcome Meek's theorem that states that, in two dimensions, all extrema in electric field magnitude occur at zero electric field.

The first guide we consider is a helical guide formed from two twisted wires (Fig. 4.1.a). This guide is likely to be useful for manipulating low field seeking states without a loss of alignment, but is unlikely to be useful in an e-EDM measurement: Molecules traversing the beam will accumulate a large trajectory-dependent geometric phase. This phase would cause rapid loss of coherence in an optically polarized beam transversing the guide.

The second guide is a Stark gravitational guide formed from two slightly distorted plates (Fig. 4.1.b). This guide offers simplicity of construction. More importantly, because the trap is created from fields restricted to two dimensions, no geometric phase will accumulate within the guide. However trap acceptance is limited by the size of the gravitational acceleration g, with an acceptance of 6×10^{-7} sr for a 200 m/s beam of ground state of $^{208}Pb^{19}F$ molecules.

The final guide we present is the cylindrical guide (Fig. 4.1.c). This guide is a dynamical guide of high-field seeking states. The trap is also created by a two-dimensional field, so decoherence due to the accumulation of a geometric phase within the guide is not expected. In addition, the effective guide depth is very deep, leading to an acceptance of 3×10^{-4} sr for a 200 m/s beam of ground state $^{208}Pb^{19}F$ molecules. If difficulties associated with its precise construction can be overcome, this guide may prove the best candidate for a long coherence time guided e-EDM experiment.

4.4 The Optical Double Resonance Quantum Beat Measurement of the e-EDM

In the near future, we plan to carry out an optical double resonance quantum beat measurement of the e-EDM. By implementing the Stark biased guide, the experiment can be conceived as in Fig. 4.7. The experimental setup can be divided into three regions. The first region is the state preparation region. The rotationally-cooled molecular beam of PbF is created in the source chamber

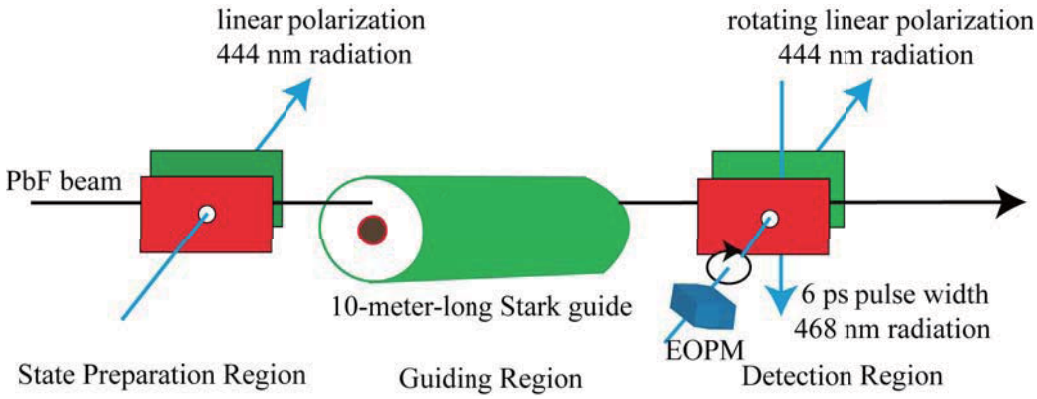

Figure 4.7: Schematic for the optical double resonance quantum beat measurement of the e-EDM.

and introduced into the detection chamber as a result of differential pumping, where the PbF molecules will be polarized by the 444 nm radiation (cw diode laser) with the polarization direction perpendicular to the electric field. The molecules will be excited from $X_1(v = 0, J = 1/2, |M_F| = 1, F = 1)$ state to $A(v = 0, J = 1/2, M_F = 0, F = 1)$ state. Please notice that the vibrational transition band has been changed. In Chapter 3, we used the vibrational state $A(v = 1)$ for the measurement of the molecular dipole moments. However, we replaced diode laser later and with the new diode laser system, we moved to the observance of the spectra of $X_1(v = 0) \rightarrow A(v = 0)$ transition. The decay of the A state will result in the generation of the coherent superposition state $|\psi\rangle = \frac{1}{\sqrt{2}}(|1\rangle + |-1\rangle)$, where $|\pm 1\rangle$ indicate the $M_F = \pm 1$ states. Once the superposition state is created, the molecules will enter the second region: the Stark guiding region. In this experimental setup, a high-field seeking cylindrical guide is implemented, whose gradient field can prevent the molecular beam

from diverging. We also notice that in the cylindrical guide, the relatively high electric field in the guiding path can fully polarize the PbF molecule, which will gain much sensitivity to the e-EDM measurement. Because the molecules leave the state preparation region with a state $|\psi\rangle = \frac{1}{\sqrt{2}}(|1\rangle + |-1\rangle)$, during their journey along the cylindrical guide, a sum of quantum phase will be accumulated due to several phase factors, the e-EDM phase ϕ_{EDM}, the phase due to background magnetic field ϕ_B and the geometric phase ϕ_Ω. Therefore, after leaving the guide, the quantum state of the ground state PbF molecules will become

$$|\psi\rangle = \frac{1}{\sqrt{2}}(|1\rangle + e^{-\imath\phi}|-1\rangle), \tag{4.24}$$

where,

$$\phi = \phi_{EDM} + \phi_B + \phi_\Omega. \tag{4.25}$$

Here, $\phi_{EDM} = d_e E_{eff}\tau/\hbar$, $\phi_B = g\mu_B\tau/\hbar$, and ϕ_Ω needs to be determined by the real experimental setup. The molecule of the accumulated quantum state will finally enter the detection region. In the detection region, we still use the pc-REMPI detection scheme, which is illustrated in Chapter 3. However, due to the change of the diode laser system, the vibronic detection scheme is

$$X_1(v=0) \rightarrow A(v=0) \rightarrow D(v=0) \rightarrow PbF^+/e^-. \tag{4.26}$$

In order to detect the signal and control the systematic errors, we add an electro-optic phase modulator (EOPM, Thorlabs, EO-PM-NR-C4) to modulate

the polarization direction of the diode laser into the detection region. The modulation will result in a rotating linear polarized light, which can dynamically excite the $X_1(v=0) \rightarrow A(v=0)$ transition. In other words, it will add an modulation phase into the accumulated quantum phase, therefore the total phase would be

$$\phi = \phi_{EDM} + \phi_B + \phi_\Omega + \phi_D, \tag{4.27}$$

where ϕ_D represents the phase due to the modulation. Rapid demodulation of ϕ_D (in orders of kHz) will lead to a precise measurement of the $\phi_{EDM} + \phi_B + \phi_\Omega$. If we reverse the direction of external electric field back and forth and demodulate the total quantum phase, we will have

$$\phi = \pm\phi_{EDM} + \phi_B + \phi_\Omega. \tag{4.28}$$

Assuming the ideal detection efficiency, the signal intensity will be

$$\begin{aligned} I_{sig} &\propto \cos^2(\pm\phi_{EDM} + \phi_B + \phi_\Omega) \\ &\propto \cos[2(\pm\phi_{EDM} + \phi_B + \phi_\Omega)]. \end{aligned} \tag{4.29}$$

The signal pattern of Eq. 4.29 can be conceived as in Fig. 4.8.

From Fig. 4.8, we can easily prove that the e-EDM signal would be obtained from the following equation

$$d_e = \frac{\hbar\Delta\phi}{4E_{eff}\tau}. \tag{4.30}$$

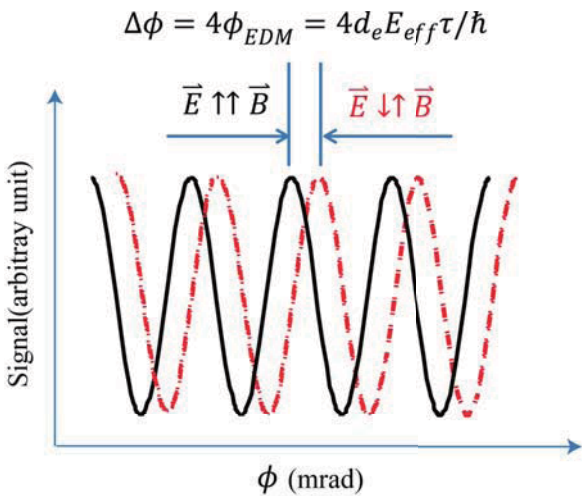

Figure 4.8: Ideal pattern of demodulated e-EDM signal of the reversing electric field. The solid line is the signal pattern for $\vec{E}||\vec{B}$, while the dashed line is the signal pattern for $-\vec{E}||\vec{B}$.

Practically, we modulate ϕ_D to allow for a total phase of $\pi/4$ with respect to the sum of ϕ_B, ϕ_Ω and ϕ_D. Therefore, I_{sig} will obtain a linear dependence of the e-EDM phase. The peak difference in Fig. 4.8 can schematically show how the e-EDM phase relates to the phase difference, but in a real experiment, the peaks of the signal are not sensitive t the phase measurement. We are still interested in the signal in linear dependence of the e-EDM phase.

4.5 Estimate of the Statistical Sensitivity of the e-EDM Measurement

From the experimental setup Fig. 4.7, we can estimate the statistical uncertainty and demonstrate how well we can improve our e-EDM limit comparing with the current limit. I list the parameters in the Tab. 4.1, and some parameters

such as the production rate of the molecular source come from other molecular e-EDM group since we can implement a similar source, while some parameters such as detection efficiency come from our previous experimental results.

Variable	Value	Explanation of the variable
E_{guide}	$50,000 V/cm$	Electric field at the center of the guide
A_{probe}	0.01 cm^2	Focal area of the probe laser
A_{guide}	0.785398 cm^2	Approximated area of the guide
Δx	0.01 cm	Effective x-acceptance of the apparatus
Δy	0.3 cm	Effective y-acceptance of the apparatus
Δx_{pump}	0.01 cm	Min. of x-focal size of pump laser and guide acceptance
Δy_{pump}	0.3 cm	Min. of y-focal size of pump laser and guide acceptance
$\Delta v_{x,guide}$	2 m/s	vx-acceptance of the guide
$\Delta v_{y,guide}$	8 m/s	vy-acceptance of the guide
L_{guide}	10 m	Length of the guide
v_{beam}	200 m/s	From the ACME group[61]
N_{source}	$1. \times 10^{10}$	Particles/shot/quantum state from ACME group[61]
f_{source}	100 s^{-1}	Repetition rate of the laser ablation source
$\Delta\Omega_{source}$	0.1	Divergence of source from ACME group[61]
d	200.0 cm	Distance from the source to the guide entrance
Eff	0.3	Efficiency of ion/e- detection
$DetectRate$	2864.79 s^{-1}	Predicted detection rate
$T_{measurement}$	86400 s	Time of measurement
τ	0.05 s	Coherence time of measurement
ν_{edm}	0.015 Hz	Frequency of e-EDM measurement at $10^{-27} e \cdot cm$
$\delta\phi$	0.0188496	Field reversal angle change at $10^{-27} e \cdot cm$
$CPsensitivity$	0.0134883	Statistical sensitivity in units of $10^{-27} e \cdot cm \cdot day^{1/2}$

Table 4.1: Estimate of the e-EDM statistical sensitivity of a 10-m-long guide.

From the proposed experimental setup, we have a estimate of statistical sensitivity of $1.345 \times 10^{-29} e \cdot cm$ for a data-taken time of a single day. Comparing the result with the current limit $d_{e,stat} = 5.7 \times 10^{-28} e \cdot cm$, this estimated result can improve the statistical sensitivity by a factor of 50 in a single day.

4.6 Conclusion

In this chapter, I talk about three possible Stark biased guides and compare their features for our proposed e-EDM measurement and conclude that the cylindrical Stark guide is the best one if the difficulties of the construction can be overcome. By implementing the cylindrical guide into the optical double resonance quantum beat experimental, I demonstrate a simple setup showing how we can measurement the e-EDM signal. Based on that, the estimate of the statistical sensitivity of the setup is performed and I prove that the sensitivity can be improved approximately by a factor of 50 in a data-taken time of a signal day. All of these results imply that the PbF molecular e-EDM measurement is a promising experiment of measuring the non-zero e-EDM.

Chapter 5

Comment on: Possibility of Zero-g-factor Paramagnetic Molecules for the Measurement of the Electron's Electric Dipole Moment

PbF has an electric-field-dependent g-factor for its ground state $^2\Pi_{1/2}$. In the literature published before, this g-factor can be tuned to zero at a certain electric field. However, a discrepancy of the hyperfine constant $A_{\perp,X_1}$ between theory and experiment has been discovered. This discrepancy can be resolved by a sign change in the phase factor between two Ω-doublet states for the ground state of the molecule. This phase factor can further influence our conclusion about the zero g-factor prediction. In this chapter, we will re-evaluate the g-factor with the corrected quantum basis set, and comment on the possibility of a zero-g-factor for the e-EDM measurement of PbF.

5.1 Introduction

In Chapter 2 and Chapter 3, we discussed the numerous experimental and theoretical studies in determining the energy level structure of the PbF molecule. All these efforts are motivated by the belief that, PbF is an important candidate for measuring the e-EDM. For this heavy paramagnetic molecule, Dr. Neil Shafer-Ray showed that $^{208}Pb^{19}F$ has a possible zero-g-factor when the external electric field is 68 kV/cm[62]. If true, this feature will greatly reduce the sensitivity of the e-EDM measurement to the background magnetic field. After

this work, our group McRaven *et al.*[17] measured the hyperfine level structure of the ground state X_1 of the $^{207}Pb^{19}F$ molecule, and found it disagreed with the theoretical predictions by Kozlov *et al*[24][43]. This theoretical mistake was eventually tracked to the wrong designation of the electronic parities[52]. Here we address the impact of this mistake on the possible vanishing g-factor of the $^{208}Pb^{19}F$.

5.2 Theory

5.2.1 Effective Spin-Rotational Hamiltonian and the Choices of the Basic Sets in the Two Coordinate Frames

Let's start by reviewing how energy levels of $^{208}Pb^{19}F$ are determined. The evaluation of PbF energy levels originate from constructing the effective spin-rotational Hamiltonian. The complete form can be obtained from Ref.[44] or modified from Eq. 2.42

$$H_{sr} = B\mathbf{J}^2 + \Delta\mathbf{S}' \cdot \mathbf{J} + \mathbf{I} \cdot \hat{\mathbf{A}} \cdot \mathbf{S}' + (W^d d_e)\mathbf{S}' \cdot \mathbf{n} - D\mathbf{E} \cdot \mathbf{n} + \mu_B \mathbf{B} \cdot \hat{\mathbf{G}} \cdot \mathbf{S}'. \quad (5.1)$$

Here we keep the same sign for the second term as the one in Ref. [44]. The first term is the rotational energy, the second term gives rise to the Ω-doubling with Δ denoting as the Ω-doubling constant, the third term gives the hyperfine interaction, the fourth term gives the interaction of the e-EDM with the internal field of the molecule, the fifth and sixth term give the interaction with an applied

electric field and magnetic field respectively. The basis set in the lab-based frame can then be expressed as[22]

$$|FIJM_F p\rangle = \sum_{M_J, M_I} \langle IM_I JM_J|FM\rangle |JM_J p\rangle |IM_I\rangle. \tag{5.2}$$

For the ground state of $^{208}\mathrm{Pb}^{19}\mathrm{F}$ $^2\Pi_{1/2}(|\Lambda| = 1, |\Omega| = \frac{1}{2})$, we introduce the pseudo-angular-momentum operator $\mathbf{S}^{prime}$ in the degenerate subspace $|\Omega\rangle$[43], where

$$\mathbf{S}'|\Omega\rangle = \Omega|\Omega\rangle. \tag{5.3}$$

Here, we need to pay careful attention to the space inversion operator $\tilde{\mathbf{P}}$ in the molecule-based frame. In the case of the PbF molecule with one free electron, the space inversion operator transforms the electronic-rotational wave function in the molecule-based frame into its opposite $|\Omega\rangle$ state with a phase factor $(-1)^{J-1/2}$ [19][52]

$$\tilde{\mathbf{P}}|FIJM_F, \Omega\rangle = (-1)^{J-1/2}|FIJM_F, -\Omega\rangle. \tag{5.4}$$

We notice that although $\tilde{\mathbf{P}}$ cannot transform the wave function into its eigenfunction, the eigenfunction can still be formed by an appropriate combination of $|\Omega = \frac{1}{2}\rangle$ states. Thus, we can represent the basis set Eq. 5.2 of a definite

parity in the molecule-based frame as[22]

$$|FIJM_F p\rangle = \frac{1}{\sqrt{2}}(|FIJM_F, \Omega = \frac{1}{2}\rangle + p(-1)^{J-1/2}|FIJM_F, \Omega = -\frac{1}{2}\rangle). \quad (5.5)$$

While in Ref. [43], the phase factor is taken as $(-1)^{J+1/2}$. This is the origin of the discrepancy of the theoretical prediction[24][43] and experimental result[17] of $A_{\perp,X_1}$. Let's re-evaluate the effective spin-rotational Hamiltonian to reveal the effect of this correction.

5.2.2 Field-free Effective Hamiltonian

In order to model the impact on the g-factor, let's consider only the rotational and the fine structure term of the effective Hamiltonian. We neglect the hyperfine effects so that J is still a good quantum number. Pseudo-spin $|\Omega\rangle = |\pm\frac{1}{2}\rangle$ will be the only mixed quantum state. Therefore, the basis set of a definite parity will be written as

$$|JM_J p\rangle = \frac{1}{\sqrt{2}}(|JM_J, \Omega = \frac{1}{2}\rangle + p(-1)^{J-1/2}|JM_J, \Omega = -\frac{1}{2}\rangle). \quad (5.6)$$

Before we figure out the impact of the phase factor on the Ω-doubling term, we can replace Δ by $\pm\Delta$ such that the secular equation can be expressed as

$$\langle J'M'_J\Omega'|H_{rot}|JM_J\Omega\rangle = \langle J'M'_J\Omega'|B\mathbf{J}^2 + \pm\Delta\mathbf{S}'\cdot\mathbf{J}|JM_J\Omega\rangle \tag{5.7}$$

$$= \delta_{JJ'}\delta_{M_JM'_J}((BJ(J+1) - \frac{\pm\Delta}{4})\delta_{\Omega\Omega'} \tag{5.8}$$

$$+ \frac{\pm\Delta}{4}(2J+1)\delta_{\Omega,-\Omega'}). \tag{5.9}$$

The $\pm$ sign in the off-diagonal term indicates the ground state $J = \frac{1}{2}$ is in either the positive or the negative combination of the $|\Omega = \pm\frac{1}{2}\rangle$ states. The energy levels can then be obtained

$$\begin{aligned} U_{tot} &= U_e + U_{vib} + U_{rot} && (5.10)\\ &= T_v + BJ(J+1) - \frac{\pm\Delta}{2}(J+\frac{1}{2}) + (\frac{\pm\Delta}{4}) && (5.11)\\ &= BJ(J+1) - \frac{\pm\Delta}{2}(J+\frac{1}{2}) + (T_v + \frac{\pm\Delta}{4}), && (5.12) \end{aligned}$$

We can determine the term $T_v + \frac{\pm\Delta}{4}$ experimentally, however, the electronic and vibrational energy are not known accurately enough to get the sign correctly in this way. Actually from the corrected form of the basis set in Eq. 5.6, the secular equation in the lab-based frame will be displayed as

$$\begin{aligned} \langle J'M'_Jp'|B\mathbf{J}^2 + \Delta\mathbf{S}'\cdot\mathbf{J}|JM_Jp\rangle = \delta_{JJ'}\delta_{M_JM'J}\delta_{pp'}(BJ(J+1) + \frac{\Delta}{4} \\ - p(-1)^{J-1/2}\frac{\Delta}{2}(J+\frac{1}{2})). \end{aligned} \tag{5.13}$$

It can be easily shown that the energy level structure with a definite parity is

$$U(J, M, p) = BJ(J+1) - p(-1)^{J-1/2}\frac{\Delta}{2}(J+\frac{1}{2}) + \frac{\Delta}{4}. \tag{5.14}$$

Now we match Eq. 5.14 with Eq. 5.12. Since Δ is negative[44] and the lower energy level is odd parity, by comparing Eq. 5.14 with Eq. 5.12, we can immediately determine that -Δ will be selected and the secular equation for the true ground state is actually the asymmetric combination of the Ω-doublet states. The secular equation in the molecule-based frame of the real ground state is then expressed as

$$\langle J' M'_J \Omega' | H_{rot} | J M_J \Omega \rangle = \delta_{JJ'}\delta_{M_J M'_J}((BJ(J+1) + \frac{\Delta}{4})\delta_{\Omega\Omega'} - \frac{\Delta}{4}(2J+1)\delta_{\Omega,-\Omega'}). \tag{5.15}$$

From this derivation, we can find that the error in the phase factor $(-1)^{J-1/2}$ of the real ground state is the cause for different secular equations, which has a direct impact on our energy level structure. In this case, if we conform to the definition of Δ, we need to rewrite the Eq. 5.1 as

$$H_{sr} = B\mathbf{J}^2 - \Delta\mathbf{S}' \cdot \mathbf{J} + \mathbf{I} \cdot \hat{\mathbf{A}} \cdot \mathbf{S}' + (W^d d_e)\mathbf{S}' \cdot \mathbf{n} - D\mathbf{E} \cdot \mathbf{n} + \mu_B \mathbf{B} \cdot \hat{\mathbf{G}} \cdot \mathbf{S}'. \tag{5.16}$$

5.2.3 Field-dependent Effective Hamiltonian

With the corrected phase factor in the wave function, we now need to consider the field-dependent effective spin-rotational Hamiltonian. In our e-EDM experiment,

the magnetic field interaction will be regarded as a perturbation with respect to the rotational energy levels with fine structure and the electric field interaction, since our quality magnetic shielding can reduce the influence of the background magnetic field dramatically. For simplification, we define our z axis to lie along the electric field vector direction. Therefore, the matrix elements of the Stark interaction in the $|JM_J\Omega\rangle$ basis is(Eq. 2.40)

$$\langle J'M'_J\Omega'|H_E|JM_J\Omega\rangle = \langle J'M'_J\Omega'| - D\hat{n}\cdot\mathbf{E}|JM_J\Omega\rangle \tag{5.17}$$

$$= DE(-1)^{J+\Omega}\sqrt{(2J+1)(2J'+1)} \times \begin{pmatrix} J' & 1 & J \\ \Omega' & 0 & -\Omega \end{pmatrix} \times (-1)^{J'-M'_J} \begin{pmatrix} J' & 1 & J \\ -M'_J & 0 & M_J \end{pmatrix}. \tag{5.18}$$

The matrix representation of the Hamiltonian without a perturbation for $J = \frac{1}{2}$, $M_J = \frac{1}{2}$ and $\Omega = \pm\frac{1}{2}$ is

$$\langle J'M'_J\Omega'|H_0|JM_J\Omega\rangle = \langle J'M'_J\Omega'|H_{rot} + H_E|JM_J\Omega\rangle \tag{5.19}$$

$$= \begin{pmatrix} \frac{3}{4}B + \frac{1}{4}\Delta + \frac{1}{3}DE & -\frac{1}{2}\Delta \\ -\frac{1}{2}\Delta & \frac{3}{4}B + \frac{1}{4}\Delta - \frac{1}{3}DE \end{pmatrix}. \tag{5.20}$$

For the weak magnetic field background, the Zeeman interaction will be treated as a small perturbation. The matrix elements of the Zeeman interaction can be

shown as(Eq. 2.38)

$$\begin{aligned}\langle J'M'_J\Omega'|H_B|JM_J\Omega\rangle &= \langle J'M'_J\Omega'|\mu_B\mathbf{B}\cdot\hat{G}\cdot\mathbf{S}'|JM_J\Omega\rangle \\ &= \mu_B\sum_{s,t}(-1)^{J+J'-1/2-M_J}G_tB_s^1\sqrt{\frac{3}{2}(2J+1)(2J'+1)} \\ &\begin{pmatrix}1/2 & 1 & 1/2\\ \Omega' & t & -\Omega\end{pmatrix}\begin{pmatrix}J' & 1 & J\\ \Omega' & t & -\Omega\end{pmatrix}\begin{pmatrix}J & 1 & J'\\ -M_J & s & M'_J\end{pmatrix}.\end{aligned} \tag{5.21}$$

Here, s and t range from -1 to 1, $G_0 = G_{||}$, $G_{\pm1} = G_\perp$, $B_0^1 = B_z$, and $B_{\pm1}^1 = \mp(B_x \pm iB_y)/\sqrt{2}$. For a strong electric field, $B_\pm$ does not contribute to the first-order Zeeman effect[28]. Therefore we only need to consider the B_z contribution. Again, the matrix representation of the perturbation for $J = \frac{1}{2}$, $M_J = \frac{1}{2}$ and $\Omega = \pm\frac{1}{2}$ is

$$\langle J'M'_J\Omega'|H_B|JM_J\Omega\rangle = \begin{pmatrix}\frac{1}{6}\mu_BB_zG_{||} & \frac{1}{3}\mu_BB_zG_\perp\\ \frac{1}{3}\mu_BB_zG_\perp & \frac{1}{6}\mu_BB_zG_{||}\end{pmatrix}. \tag{5.22}$$

5.2.4 Evaluation of the *g*-factor

As we have the Hamiltonian without the perturbation, H_0, Eq. 5.19 and the first-order perturbation, H_B, Eq. 5.22, from the first-order perturbation theory, we have the definition of the g-factor as

$$g_i = \frac{\langle e_i|H_B|e_i\rangle}{\mu_BB_zM_J}. \tag{5.23}$$

Here, $|e_i\rangle$ is an eigenvector of H_0 and $M_J = \frac{1}{2}$. As we mentioned above, there are two eigenvectors correspond to the Hamiltonian, one is the anti-symmetric combination of the $|\Omega = \frac{1}{2}\rangle$ states and the other one is the symmetric combination. The anti-symmetric combination represents the ground state with odd parity, which is the true ground state. Incorporating the correct eigenvector (odd parity), we will get the g-factor as

$$g = \frac{1}{3}G_{||} + \frac{2\Delta}{\sqrt{9\Delta^2 + 4D^2E^2}}G_{\perp}. \tag{5.24}$$

This result is similar to the result published in Ref. [62], except for a sign discrepancy between the two terms. This discrepancy can be easily removed, as we discussed before, by replacing Δ with $-\Delta$. Provided the negative product relation

$$G_{\perp}G_{||}\Delta < 0, \tag{5.25}$$

we can obtain a vanishing g-factor as the electric field increases if these parameters of ^{208}Pb^{19}F satisfy the above relation. Unfortunately, since $G_{||} > 0$, $G_{\perp} < 0$ and $\Delta < 0$[22] we have a positive product. From Eq. 5.24 we see that it is unlikely for ^{208}Pb^{19}F to reach a vanishing limit. One might be interested in the g-factor for the excited Ω-doublet state, since this state is the eigenstate incorporated into perturbation theory which yields a vanishing g-factor. However, for the excited Ω-doublet state, the minimal J-mixing assumption isn't valid since the high-J levels will mix strongly in the electric field. In

either situation, we will never get a vanishing g-factor for $^{208}Pb^{19}F$ regardless of the amplitude of the large electric field (Fig. 5.1). Careful analysis of the rich hyperfine structure for $^{207}Pb^{19}F$ shows that, for several electric fields, a vanishing g-factor is possible. However, these states are about ten times less sensitive to an e-EDM at the electric fields where the g-factor minimizes.

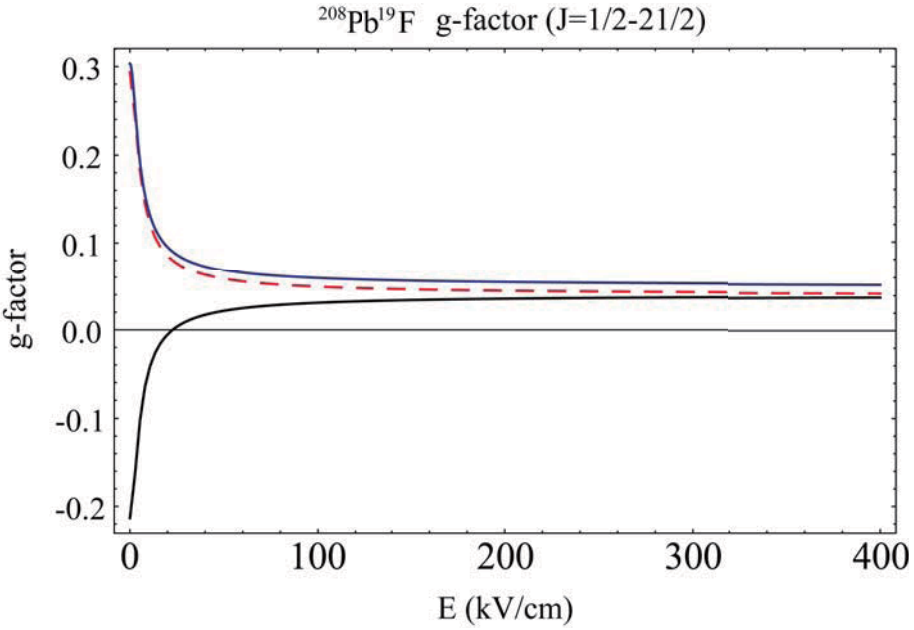

Figure 5.1: Comparison of the g-factors for the ground Ω-doublet state (upper line), the excited Ω-doublet state (lower line) and the analytical result (medium dashed line). J-state mixes from $\frac{1}{2}$ to $\frac{21}{2}$.

Although the zero g-factor does not exist in $^{208}Pb^{19}F$, the g-factor is still small. As the external electric field increases, the g-factor approaches $\frac{1}{3}G_{||}$, a number on the order of $g_e - 2$. From Ref. [22], $G_{||}$ is approximately 0.12, therefore we can obtain a g-factor as low as 0.04. Additionally, the perturbation from the background magnetic field will be further suppressed by the high quality magnetic shielding. With the feature of the great enhancement factor

of PbF, the contribution of the background magnetic field to the e-EDM is minor. To prove that, we estimate the variation of the quantum phase due to the background magnetic field as

$$\Delta\phi_B = \frac{10\% \times 2\pi g \mu_B B \tau}{\hbar}. \tag{5.26}$$

Here, 10% is caused by the variation of the electric field. In order to gain a sensitive measurement, we prove in Chapter 4 that $\Delta\phi_B$ should be restricted below $\pi/4$. If we take $g = 0.1$ and coherence time $\tau = 5s$, we should guarantee that the background magnetic field would be less than 0.28 μG. In the near future, we will implement a quality μ-metal shielding and a superconducting shielding to effectively reduce the magnetic field down to 0.1 μG. This result shows that the small non-vanishing g-factor can still lead to an e-EDM measurement using the PbF molecule.

5.3 Conclusion

In summary, a sign error in the phase factor appearing in Ref.[17] led to both a disagreement between theory and the first observed hyperfine energy level structure of the $^{207}Pb^{19}F$ molecule. Failure to catch this error also led the author of Ref. [62] we are commenting on to falsely predict the existence of a vanishing magnetic moment of the ground state of the $^{208}Pb^{19}F$ molecule. It is emphasized that although the magnetic moment of the ground state $^{208}Pb^{19}F$

does not vanish at a certain value of electric field, it does approach to 0.04 in the strong electric fields, a value low enough to perform a competitive e-EDM experiment.

Chapter 6

Summary

It has been 62 years since Purcell and Ramsey initiated the search for the permanent EDMs of fundamental particles. And it is almost 10 years since our group started the experimental search for the e-EDM. One can tell all the progress our group has made from the group publications and theses of Dr. Sivakumar Poopalasingam, Dr. Chris McRaven and Dr. Milinda Rupasinghe. In general, the progress reported by this thesis can be summarized by these aspects.

In the first place, we made a further step in measuring the spectroscopic constants of $X_1(^2\Pi_{1/2})(\upsilon = 0)$ and $A(^2\Sigma_{1/2})(\upsilon = 1)$ states of $^{208}Pb^{19}F$. The spectra, archived in a pc-REMPI detection scheme, can be analyzed efficiently under the model of effective spin-rotational Hamiltonian. Also, the results indicate some improvements that can help obtain a higher count rate, and better spectral resolution. Now a tunable, frequency-doubled, high power diode laser with excellent thermal and mechanical stability has been implemented in our system, and the resolution of the probed transition can be enhanced by a factor of 5, approximately.

Secondly, we proposed three possible Stark guides that overcome Meek's theorem and can enhance the coherence time in the optically-doubled resonance measurement of the e-EDM. The helical guide will accumulate a geometric phase during the traveling of the molecule, and the gravitational guide is easy to

construct but has a fairly low acceptance. Given that the difficulties associated with its precise construction can be overcome, the cylindrical guide might be the most appropriate one in the long coherence time guided e-EDM experiment, due to its large acceptance and less accumulation in the geometric phase.

Thirdly, we resolved the discrepancy between theory and the first observed hyperfine energy level structure of the $^{207}Pb^{19}F$ molecule. This will lead to the proposal of a zero-g-factor e-EDM measurement. We reviewed the analysis carefully and determined that all these mishaps came from the sign error of the relative phase between the $|\Omega = \pm\frac{1}{2}\rangle$ degenerate states. We found that, although the magnetic moment of the ground state $^{208}Pb^{19}F$ does not vanish at a certain value of electric field, it does become very small in strong electric fields, approaching a value of 0.04. This small value of the g-factor, combined with quality magnetic shielding, can still lead us to the proposed e-EDM measurement using the PbF molecule.

In conclusion, all of the progress, as well as the group publications and theses, will lead us to yield a sensitivity of the e-EDM measurement: $1.345 \times 10^{-29} e{\cdot}\mathrm{cm}/\sqrt{day}$. These efforts will help us to compete with other e-EDM measurement groups, in a race to discover the nonzero value of the e-EDM.

References

[1] E. M. Purcell and N. F. Ramsey, On the Possibility of Electric Dipole Moments for Elementary Particles and Nuclei, Phys. Rev. Lett. 78, 807-807, 1950.

[2] T. D. Lee and C. N. Yang, Question of Parity Conservation in Weak Interactions, Phys. Rev. Lett. 104, 254-258, 1956.

[3] C.S. Wu, E. Ambler, R.W. Hayward, D.D. Hoppes, and R.P. Hudson, Experimental Test of Parity Conservation in Beta Decay, Phys. Rev. Lett. 105, 1413-1415, 1957.

[4] J. H. Christenson, J. W. Cronin, V. L. Fitch, and R. Turlay, Evidence for the 2π Decay of the K_2^0 Meson, Phys. Rev. Lett. 13, 138-140, 1964.

[5] http://www.lbl.gov/abc/wallchart/chapters/05/2.html.

[6] I. B. Khriplovich, and S. K. Lamoreaux, CP violation without strangeness: electric dipole moments of particles, atom and molecules, Springer: New York, 1997.

[7] Maxim Pospelov, Adam Ritz, Electric dipole moments as probes of new physics, High Energy Physics - Phenomenology, 62 pages, 2005.

[8] J. H. Smith, E. M. Purcell and N. F. Ramsey, Experimental Limit to the Electric Dipole Moment of the Neutron, Phys. Rev. Lett. 108, 120-122, 1957.

[9] C. A. Baker, D. D. Doyle, P. Geltenbort, K. Green, M. G. D. van der Grinten, P. G. Harris, P. Iaydjiev, S. N. Ivanov, D. J. R. May, J. M. Pendlebury, J. D. Richardson, D. Shiers and K. F. Smith, Improved Experimental Limit on the Electric Dipole Moment of the Neutron, Phys. Rev. Lett. 97, 4 pages, 2006.

[10] J. J. Hudson,D. M. Kara,I. J. Smallman,B. E. Sauer, M. R. Tarbutt and E. A. Hinds, Improved measurement of the shape of the electron, Nature-Letter 473, 493-496, 2011.

[11] R. Arnowitt, B. Dutta and Y. Santoso, Supersymmetric phases, the electron electric dipole moment and the muon magnetic moment, Phys. Rev. D 64, 12 pages, 2001.

[12] Shahida Dar, The Neutron EDM in the SM : A Review, High Energy Physics - Phenomenology, 37 pages, 2000.

[13] S. Abel, S. Khalil, O. Lebedev, EDM Constraints in Supersymmetric Theories, High Energy Physics - Phenomenology, 34 pages, 2001.

[14] W. C. Griffith, M. D. Swallows, T. H. Loftus, M. V. Romalis, B. R. Hecke and E. N. Fortson, Improved Limit on the Permanent Electric Dipole Moment of ^{199}Hg, Phys. Rev. Lett. 102, 4 pages, 2009.

[15] L. I. Schiff, Measurability of Nuclear Electric Dipole Moments, Phys. Rev. Lett. 132, 2194-2200, 1963.

[16] P. G. H. Sandars, Measurability of the Proton Electric Dipole Moment, Phys. Rev. Lett. 19, 1396-1398, 1967.

[17] C. P. McRaven, P. Sivakumar and N. E. Shafer-Ray, Experimental determination of the hyperfine constants of the X_1 and A states of $^{207}Pb^{19}F$, Phys. Rev. A 78, 4 pages, 2008.

[18] F. Hund, Handbuch der Physik, 4, 561, 1933.

[19] John Brown and Alan Carrington, Rotational Spectroscopy of Diatomic Molecules, Cambridge University Press, Cambridge, 2003.

[20] Richard N. Zare, Angular momentum: Understanding spatial aspects in Chemistry and Physics, Wiley Interscience, New York, 1988.

[21] Gordon W. F. Drake (Ed.), Springer Handbook of Atomic, Molecular and Optical Physics, Springer, New York, 2006.

[22] Richard J. Mawhorter, Benjamin S. Murphy, Alexander L. Baum, Trevor J. Sears, T. Yang, P. M Rupasinghe, C. P. McRaven, N. E. Shafer-Ray, Lukas D. Alphei and Jens-Uwe Grabow, Characterization of the ground X_1 state of $^{204}Pb^{19}F$,$^{206}Pb^{19}F$, $^{207}Pb^{19}F$, and $^{208}Pb^{19}F$, Phys. Rev. A 84, 12 pages, 2011.

[23] M. Born and R. Oppenheimer, On the quantum theory of molecules, Chapter 1.

[24] Yu. Yu. Dmitriev, Yu. G. Khait, M. G. Kozlov, L. N. Labzovsky, A. O. Mitrushenkov, A. V. Shtoff and A. V. Titov, Calculation of the spin-rotational Hamiltonian including P- and P, T-odd weak interaction terms for HgF and PbF molecules, Physics Letters A 167, 280-286, 1992.

[25] Edmund R. Meyer and John L. Bohn, Prospects for an electron electric-dipole moment search in metastable ThO and ThF^+, Phys. Rev. A 78, 010502(R), 2008.

[26] Eugene D. Commins, Stephen B. Ross, David DeMille, and B. C. Regan, Improved experimental limit on the electric dipole moment of the electron, Phys. Rev. A 50, 1994.

[27] B. C. Regan, Eugene D. Commins, Christian J. Schmidt, and David DeMille, New Limit on the Electron Electric Dipole Moment, Phys. Rev. Lett. 88, 071805, 1994.

[28] J. J. Hudson, B. E. Sauer, M. R. Tarbutt and E. A. Hinds, Measurement of the Electron Electric Dipole Moment Using YbF Molecules, Phys. Rev. Lett. 89, 4 pages, 2002.

[29] A. N. Petrov, A. V. Titov, T. A. Isaev, N. S. Mosyagin, and D. DeMille, Configuration-interaction calculation of hyperfine and P,T-odd constants on ^{207}PbO excited states for electron electric-dipole-moment experiments, Phys. Rev. A 72, 022505, 2005.

[30] D. DeMille, F. Bay, S. Bickman, D. Kawall, D. Krause, Jr., S. E. Maxwell, and L. R. Hunter, Investigation of PbO as a system for measuring the electric dipole moment of the electron, Phys. Rev. A 61, 052507, 2000.

[31] M. G. Kozlov, A. V. Titov, N. S. Mosyagin, and P. V. Souchko, Enhancement of the electric dipole moment of the electron in BaF molecule, Phys. Rev. A 56, 1997.

[32] J. Lee, E.R. Meyer, R. Paudel, J.L. Bohn and A.E. Leanhardt, An electron electric dipole moment search in the $X^3\Delta_1$ ground state of tungsten carbide molecules, Journal of Modern Optics 56, 2009.

[33] Leanhardt Research Group, http://www-personal.umich.edu/ãehardt/.

[34] A.N. Petrov, N.S. Mosyagin, T.A. Isaev, A.V. Titov, Theoretical study of HfF^+ in search of the electron electric dipole moment, Phys. Rev. A 76, 030501(R), 2007.

[35] Frank Morgan, Absorption Spectra of PbF, $PbCl$ and $PbBr$, Phys. Rev. 49, 47-50, 1936.

[36] G.D.Rochester, The Band Spectra of the Lead Halides, PbF and $PbCl$, Proceedings of the Royal Society of London. Series A, Mathematical and Physical Sciences 153, No. 879, 407-421, 1936.

[37] G.D.Rochester, The Band Spectrum of Lead Fluoride (PbF). II, Proceedings of the Royal Society of London. Series A, Mathematical and Physical Sciences 167, No. 931, 567-580, 1938.

[38] D.J.W. Lumley and R.F.Barrow, Rotational analysis of the $B-X_2$, $B-X_1$ and $A-X_1$ systems of gaseous PbF, Journal of Physics B: Atomic and Molecular Physics 10, No. 8, 1537-1541, 1977.

[39] Jing Chen and Paul J. Dagdigian, Laser fluorescence study of the $Pb + F_2$, Cl_2 reactions: Internal state distribution of the $PbCl$ product and radiative lifetimes of $PbF(A, B)$ and $PbCl(A)$, Journal of Chemical Physics 96, 1030-1035, 1992.

[40] K. Ziebarth, K.D. Setzer, O. Shestakov and E.H. Fink, High Resolution Study of the $X_2^2\Pi_{\frac{3}{2}} \rightarrow X_1^2\Pi_{\frac{1}{2}}$ Fine Structure Transitions of PbF and $PbCl$, Journal of Molecular Spectroscopy 191, 108-116, 1998.

[41] R. A. Frosch and H. M. Foley, Magnetic Hyperfine Structure in Diatomic Molecules, Phys. Rev. 88, 1337-1349, 1952.

[42] I. Kopp and J. T. Hougen, Rotational Energy Levels of $\frac{1}{2}$ States and Intensities in $\frac{1}{2} - \frac{1}{2}$ Transitions - Applications to Some Heavier Hydrides, Canadian Journal of Physics 45, 2581-2596, 1967.

[43] M. G. Kozlov, V. I. Fomichev, Y. Y. Dmitriev, L. N. Labzovsky and A. V. Titov, Calculation of the P- and T-odd spin-rotational Hamiltonian of the PbF molecule, Journal of Physics B: Atomic and Molecular Physics 20, No. 19, 4939-4948, 1987.

[44] M. G. Kozlov and L. N. Labzowsky, Parity violation effects in diatomics, Journal of Physics B: Atomic, Molecular and Optical Physics 28., No. 10, 1933-1961, 1995.

[45] B. E. Sauer, Jun Wang and E. A. Hinds, Laser-rf double resonance spectroscopy of ^{174}YbF in the $X^2\Sigma^+$ state: Spin-rotation, hyperfine interactions and the electric dipole moment, The Journal of Chemical Physics 105, 1996.

[46] P. C. Condylis, J. J. Hudson, M. R. Tarbutt, B. E. Sauer and E. A. Hinds, Stark shift of the $A^2\Pi_{1/2}$ state in ^{174}YbF, The Journal of Chemical Physics 123, 2005.

[47] W.E.Ernst, J.Kändler and T.Törring, Hyperfine structre and the electric dipole moment of BaF $X^2\Sigma^+$, The Journal of Chemical Physics 84, 1986.

[48] C.P. McRaven, P. Sivakumar, N.E. Shafer-Ray, Gregory E. Hall and Trevor J. Sears, Spectroscopic constants of the known electronic states of lead monofluoride, Journal of Molecular Spectroscopy 262, 89-92, 2010.

[49] P. Sivakumar, C.P. McRaven, P.M. Rupasinghe, T.Zh. Yang, N.E. Shafer-Ray, Trevor J. Sears and Gregory E. Hall, Pseudo-continuous resonance enhanced multiphoton ionisation: application to the determination of the hyperfine constants of $^{208}Pb^{19}F$, Molecular Physics 262, 927-935, 2009.

[50] P. Sivakumar, C. P. McRaven, Dustin Combs, N. E. Shafer-Ray and Victor Ezhov, State-selective detection of the PbF molecule by doubly resonant multiphoton ionization, Phys. Rev. A 77, 5 pages, 2008.

[51] C. P. McRaven and N. E. Shafer-Ray, A reversible time-of-flight detector for use in pseudocontinuous resonance enhanced multiphoton (pc-REMPI) detection, Review of Scientific Instruments 82, 5 pages, 2011.

[52] K. I. Baklanov, A. N. Petrov, A. V. Titov and M. G. Kozlov, Progress toward the electron electric-dipole-moment search: Theoretical study of the PbF molecule, Phys. Rev. A 82, 4 pages, 2010.

[53] A. V. Titov, N. S. Mosyagin, A. N. Petrov, T. A. Isaev and D. DeMille, Study of P,T-Parity Violation Effects in Polar Heavy-Atom Molecules, Progress in Theoretical Chemistry and Physics, 2005.

[54] Evgueni Nikitin and Elena Dashevskaya, Janis Alnis and Marcis Auzinsh, E. R. I. Abraham, Brendan R. Furneaux, Mark Keil, Chris McRaven, Neil Shafer-Ray, and Richard Waskowsky, Measurement and prediction of the speed-dependent throughput of a magnetic octupole velocity filter including nonadiabatic effects, Phys. Rev. A 68, 023403, 2003.

[55] Samuel A. Meek, E. R. I. Abraham, and Neil E. Shafer-Ray, Impossibility of a biased Stark trap in two dimensions, Phys. Rev. A 71, 065402, 2005.

[56] S. K. Sekatskii and J. Schmiedmayer, Trapping polar moelcules with a charged wire, Europhys. Lett. 36, page 407-412, 1996.

[57] Rienk T. Jongma, Gert von Helden, Giel Berden and Gerard Meijer, Confining CO molecules in stable orbits, Chemical Physics Letters 270, pages 304-308, 1997.

[58] Milinda Rupasinghe and N.E. Shafer-Ray, Effect of the geometric phase on the possible measurement of the electron's electric dipole moment using molecules confined by a Stark gravitational trap, Phys. Rev. A 78, 033427, 2008.

[59] Leanhardt, A. E. and Bohn, J. L. and Loh, H. and Maletinsky, P. and Meyer, E. R. and Sinclair, L. C. and Stutz, R. P. and Cornell, E. A., High-resolution spectroscopy on trapped molecular ions in rotating electric fields: A new approach for measuring the electron electric dipole moment, J. Mol. Spectrosc. 270, N0. 1, 1-25, 2011.

[60] Titov, A. V. and Mosyagin, N. S. and Ezhov, V. F., P, T-Odd Spin-Rotational Hamiltonian for YbF Molecule, Phys. Rev. Lett. 77, No. 27, 5346, 1996.

[61] Advanced Cold Molecule Electron EDM group, http://www.electronedm.org/.

[62] Neil E. Shafer-Ray, Possibility of 0-g-factor paramagnetic molecules for measurement of the electron's electric dipole moment, Phys. Rev. A 73, 3 pages, 2006.

Appendix A

Fabry-Pérot Interferometer

Fabry-Pérot Interferometer (or Etalon) is named after Charles Fabry and Alfred Perot, and it is widely used in lasers, spectroscopy measurement and telecommunications. In the Appendix, I will describe the physical principles of the Fabry-Pérot Interferometer, and discuss its application in the measurement of the PbF spectroscopy.

Fabry-Pérot Interferometer is made of two mirrors, with two highly reflective surfaces facing each other. The two mirrors can be either curved or flat, and coated with film of high reflectivity. When illuminated by monochromatic laser rays close to the co-axis of the two mirrors, a multiple beam interference pattern will be produced near the center of the interferometer. The following schematic Fig. A.1 shows the configuration of the Fabry-Pérot Interferometer with two flat mirrors, and I will explain the theory of operation based on this schematic. And for convenience, I will use etalon to stand for Fabry-Pérot Interferometer.

Suppose the laser light has a wavelength λ, and it enters the etalon with a small angle θ near the co-axis of the etalon. The two mirrors of the etalon is spaced by a distance d. Suppose the etalon is filled with a gas medium of the index of refraction n (we can take $n = 1$ for the case of vaccum), we can calculate that the two adjacent laser rays out the etalon have a difference of the optical path length as

$$\Delta l = 2nl\cos\theta. \tag{A.1}$$

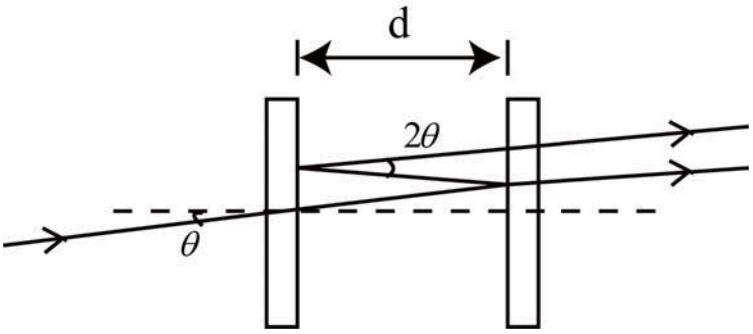

Figure A.1: Schematic of the Fabry-Pérot Interferometer made of two mirrors. The mirrors are coated with film of high reflectivity. A monochromatic and collimated laser beam enters the etalon, with a small angle θ and near the co-axis of the two mirrors.

And the phase difference would be

$$\Delta\phi = \frac{2\pi}{\lambda} 2nd\cos\theta. \tag{A.2}$$

In order to create constructive fringes, this phase difference must be integer times of 2π. Therefore, the constructive fringe pattern should satisfy the following equation

$$2nd\cos\theta = m\lambda, \tag{A.3}$$

or

$$\nu = m\frac{c}{2nd\cos\theta}. \tag{A.4}$$

Here, m is an integer number, n is the index of refraction of the medium gas, ν is the frequency of the monochromatic laser and c is the speed of light in

vacuum. We define an important parameter called free spectral range (or FSR)

$$FSR = \frac{c}{2nd\cos\theta}. \tag{A.5}$$

From Eq. A.4 we see that for every interval of FSR, the laser light can transmit through the etalon and construct the fringe pattern. In our experiment, if we sweep the grating voltage of the diode laser system, we can control the frequency of the laser into the etalon. Once the laser frequency is tuned to a value which satisfies Eq. A.4, the laser light will transmit through the etalon and captured by the photodiode detector. If we tune the frequency up by one FSR, the laser light will transmit through the etalon again, and the new frequency will have a different mode $m + 1$. By recording transmitted light intensity and the detuning laser frequency, we can keep tracking on how far we have tuned the laser system. (Actually, the grating voltage of the diode laser system is recorded, and the conversion between frequency and the grating voltage will be performed.) Fig. A.2 is a typical pattern of the transmitted light versus the laser frequency.

The etalon we use in our lab is consisted of two confocal mirrors, which is depicted in Fig. A.3. For the convenience of study, we can assume the laser light enters into the etalon closely parallel to the co-axis. This assumption can be done by manipulating of alignment and examining the interference pattern. The phase difference for the constructive interference in this case would

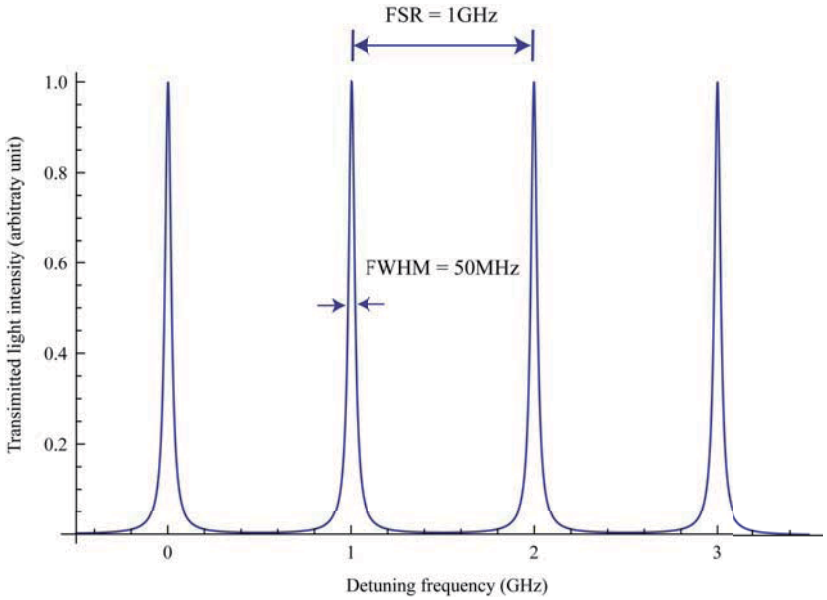

Figure A.2: A typical plot of laser transmitted light intensity versus the detuning laser frequency. The laser frequency is detuned from 674,828.0 GHz. The mirror reflectivity is 90%, and the free spectral range for the etalon is 1 GHz. The transmitted laser light has a resolution of about 50 MHz.

approximately be

$$\Delta\phi = \frac{2\pi}{\lambda} 4nd. \tag{A.6}$$

For this etalon, the FSR would be

$$FSR = \frac{c}{4nd}. \tag{A.7}$$

Here, c is the speed of the light, n is the index of refraction of the gas filled in the etalon and d is the distance between the two confocal mirrors.

There are some disadvantages and advantages between the etalon of the parallel mirrors and the etalon of the confocal mirrors. The disadvantage is,

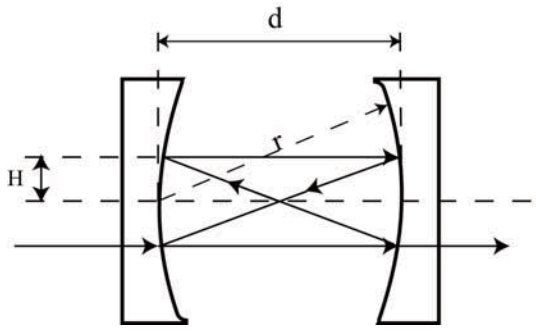

Figure A.3: The schematic of the etalon made of two confocal mirrors. The radius of the curvature of the mirror r is equivalent to the spacing d between the mirrors, therefore, the free spectral range is fixed by the choice of the mirrors.

the confocal and spherical etalon have the radius of the curvature same as the distance between the mirrors. Therefore, the confocal etalon has a fixed FSR but the parallel etalon can change its FSR much more freely. However, the confocal etalon is not as sensitive to the alignment as the parallel etalon, because it is not necessary to maintain the parallelism of the mirrors. Also, due to the confocal feature of the mirror, the laser beam will focus on the mirror surface. The focusing effect will result in smaller beam diameter, and minimize the influence on the laser beam profile due to the mirror imperfections.

Ideally, we want the spectral resolution to be as high as possible. In Fig. A.2, the spectral resolution is 50 MHz. However, the spectral resolution has several practical limitations. We introduce another important parameter of the etalon here, called finesse $\mathcal{F}$, which is given by

$$\mathcal{F} = \frac{FSR}{FWHM}, \tag{A.8}$$

where FWHM is the full width half maximum of the spectral line (or spectral resolution). We find out that, for a certain FSR, the higher the reflectivity, the higher the finesse $\mathcal{F}$, and the better the spectral resolution. However, the higher reflectivity will result in lower etalon transmission, due to the absorption of the coating film and substrate scattering losses. The $\mathcal{F}$ is also limited by how well the mirrors are fabricated and polished. The current limit of the $\mathcal{F}$ for the etalon in our lab is about 600, which will produce 1.6 MHz spectral resolution with a 1 GHz FSR.

The etalon has a very important application in the measurement of the PbF spectroscopy. The Fig. A.4 shows how we implement the etalon in the experiment, and it is also demonstrated in Fig. 3.3.

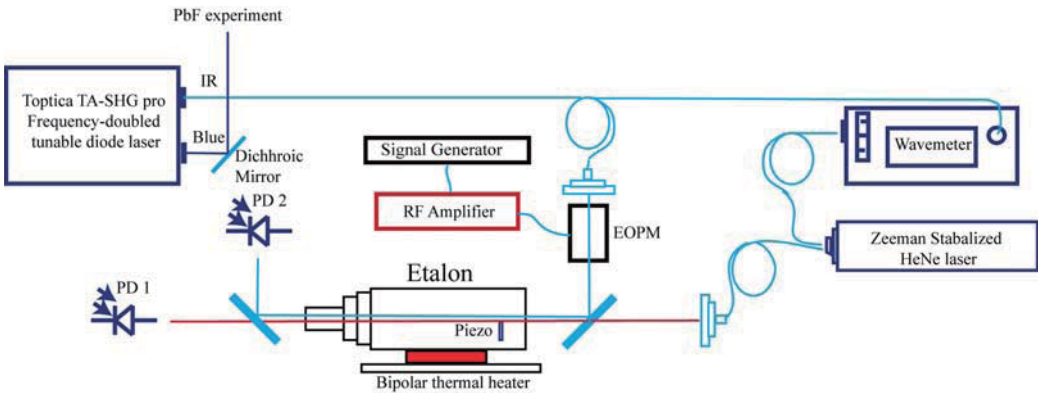

Figure A.4: The schematic of implementation of etalon in the measurement of the PbF spectroscopy.

The Zeeman-stabilized HeNe laser will be divided into two beams by the optical fiber. One beam serves as the reference beam for the wavemeter, and the other one illuminates into the etalon. Then the etalon will be locked

to the HeNe laser, and the stability of the HeNe will be transferred to the etalon. The lock mechanism works in the following way: Suppose the etalon initially has the right length to satisfy Eq. A.6. The dithering (modulated) piezoelectric transducer adjusts the length of the etalon slightly and fast, then the transmitted light intensity will be changed, due to the dithering length of the etalon and especially the other influences that we want to get rid of. The transmitted light will be collected by the photodetector, and compared with the local oscillator's signal (you can treat this as the origin of the dithering source on the piezoelectric transducer, so they share the same frequency signature) by a mixer. The function of the mixer, by implementing a low-pass filter, is to produce a low frequency signal which is essentially the derivative of the transmitted light intensity. This derivative will determine which way the length of the etalon will be changed in order to bring the transmitted light intensity back to the maximum. This is a standard lock mechanism and it is not pictured in the schematic. Also, we use a bipolar thermal heater to actively control the temperature of the etalon. All of these efforts are made that the etalon has a good stability and can be steadily locked to a certain mode indicated by the m in Eq. A.4.

Once the length of the etalon is locked, we introduce the blue laser or the fundamental IR laser into the etalon. The scanning grating voltage of the diode laser will change the frequency of the diode laser continuously, and every interval of the FSR the blue or IR laser will transmit through the etalon. For

better frequency measurement, we apply the Electro-Optic Phase Modulator (EOPM) before the blue or the IR laser entering the etalon. The function of the EOPM is to generate Radio-Frequency (RF) sidebands on top of a laser line. These sidebands are equally spaced, defined by a RF signal generator. The transmitted fringes through the etalon display as in Fig. A.5

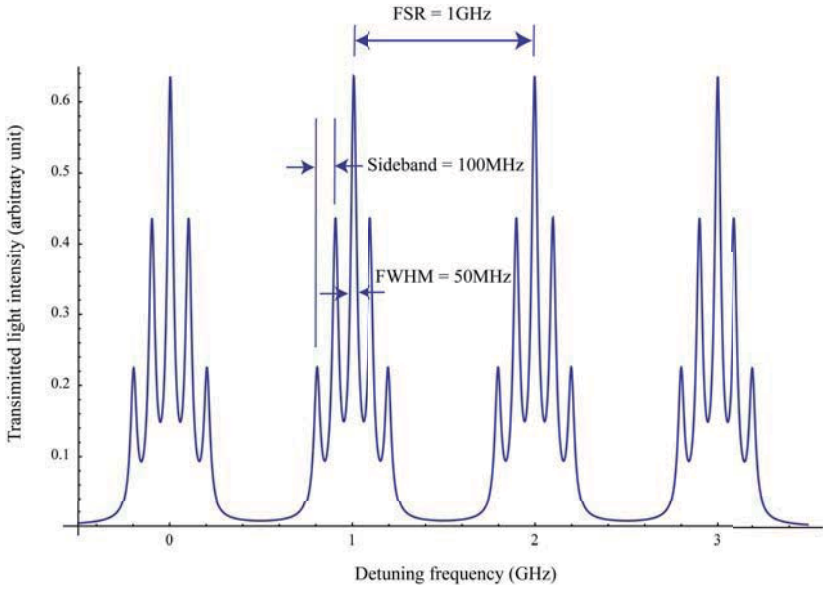

Figure A.5: A ideal plot of the transmitted fringes of the blue laser with the implementation of the EOPM. The modulation frequency is 100 MHz, therefore the sidebands are equally spaced by 100 MHz. The etalon has a FSR of 1 GHz, and the finesse $\mathcal{F}$ is 200. The number of the sidebands for each central fringe is determined by the modulation signal. The laser frequency is detuned from 674,828.0 GHz.

In Fig. A.5, there are five fringes for each pileup, and each pair of adjacent fringes are spaced by 100 MHz, which is the modulation frequency applied on the EOPM. By adjusting the RF amplifier in Fig. A.4 one can determine the number of the sidebands. In this way, one FSR can be further depicted by

these sidebands. We preliminarily scanned the rovibrational transitions of the $^{130}Te_2$ in $X_1(^3\Sigma_g) \rightarrow B_1(^3\Sigma_u)$ band near the frequency 674790.6 GHz and obtain the spectrum as Fig. A.6. We choose the spectrum of $^{130}Te_2$ for testing and

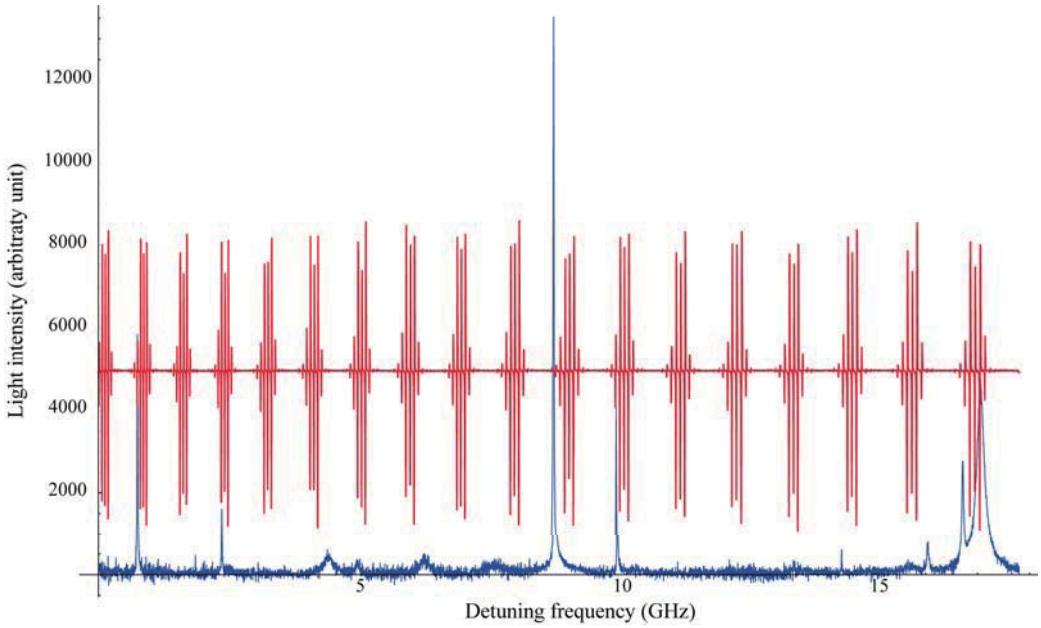

Figure A.6: Doppler-free saturated absorption spectrum of $^{130}Te_2$ in $X_1(^3\Sigma_g) \rightarrow B_1(^3\Sigma_u)$ band near the frequency 674790.6 GHz. The pileups of the fringes are the derivative of the transmitted light intensity of the blue laser. Each pileup contains the major fringe and the four sidebands. Each pair of adjacent sidebands are spaced by 90 MHz.

a reference for the PbF spectrum. In the Doppler-free saturated absorption $^{130}Te_2$ spectrum, about 18 pileups have been observed. For each pileup, there are at least four or six sidebands and the major central fringe. These sidebands can characterize the interval between two major fringes more precisely. In this case, the interval of the sidebands is 90 MHz for each pile up. If one apply the 95 MHz sidebands, and we know the positions of the major fringes won't be

changed since the etalon length is locked, you can easily determine the frequency intervals between two arbitrary lines. In the spectrum of $^{130}Te_2$, the position of an absorption line will be given by the sum of the frequency of the origin, the mode number of the main fringe, and the two sidebands the absorption line will lie between. If the frequency of the sidebands is changed, the absorption line will appear between another two sidebands, with the frequency of the origin and the mode number of the main fringe unchanged. One can easily compute the absorption line position based the differences of the sidebands. For the intervals of the arbitrary two absorption lines, we even do not need to know the origin of the frequency for the spectrum. The relative number of the mode for the etalon, and the difference of the sidebands can tell what the line interval is. And the uncertainty of the interval will rely on two factors: the frequency drift of the diode laser, and the uncertainty of the sidebands. The uncertainty of the sidebands will be produced by the RF signal generator which is in order of several Hz. And in a 48-hour-time stability test we found that the laser frequency drift is about 2 MHz. The etalon implemented in the diode laser system is proved to be a useful frequency caliper.

The second important application of the etalon in the diode laser system is: It can transfer the stability of the HeNe laser to the diode laser, by locking the blue laser to the etalon while the etalon is locked to the HeNe laser. In this case, we use pressure-tuning setup to change the index of refraction of the gas medium (Nitrogen) inside of the etalon. From Eq. A.6 and Eq. A.7, we

know that in order to maintain the etalon locked to the HeNe, the length of the etalon have to change in order to make the product $n_{HeNe}d$ unchanged. But due to the dispersion effect, the change of the index of refraction will be different for blue diode laser. Therefore, in order to lock the blue diode laser to the etalon at the same time, the frequency of the blue laser will be changed accordingly to compensate the the changes due to the dispersion and the length of the etalon. Fig. A.7 is adopted from the paper *Cavity dispersion tuning spectroscopy of tellurium near 444.4 nm*, published by Coker *et al* in Journal of the Optical Society of America B 28, December 2011. In this figure, the

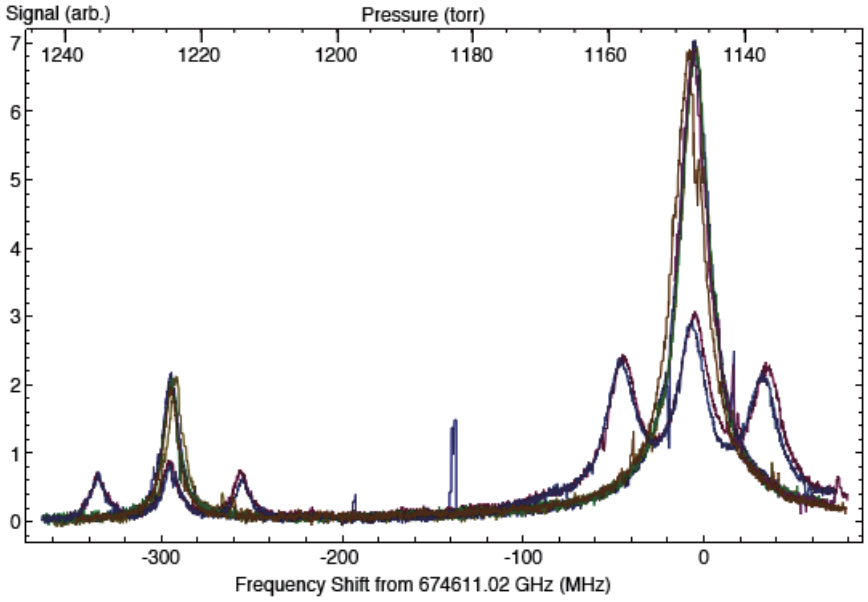

Figure A.7: Pressure-tuning of the etalon under the dispersion effect of the Nitrogen. The sideband is 40 MHz, which is applied on the probe beam of the Doppler-free saturated absorption setup. Adopted from *Cavity dispersion tuning spectroscopy of tellurium near 444.4 nm*, Coker *et al.*, J. Opt. Soc. Am. B 28, December 2011.

sideband is 40 MHz, and the interval of the two absorption lines is 289±3 MHz.

Again, this result proves that, the etalon is playing an important role in the precision measurement.